Journal of Hazardous Materials 423 (2022) 127005

Contents lists available at ScienceDirect

Journal of Hazardous Materials

journal homepage: www.elsevier.com/locate/jhazmat

H_2O_2 production at gas-diffusion cathodes made from agarose-derived carbons with different textural properties for acebutolol degradation in chloride media

Yanyu Zhang [a,b,1], Giorgia Daniel [c,1], Sonia Lanzalaco [d], Abdirisak Ahmed Isse [c], Alessandro Facchin [c], Aimin Wang [b], Enric Brillas [a], Christian Durante [c,*], Ignasi Sirés [a,*]

[a] Laboratori d'Electroquímica dels Materials i del Medi Ambient, Departament de Química Física, Facultat de Química, Universitat de Barcelona, Martí i Franquès 1–11, 08028 Barcelona, Spain

[b] Department of Municipal and Environmental Engineering, Beijing Key Laboratory of Aqueous Typical Pollutants Control and Water Quality Safeguard, Beijing Jiaotong University, Beijing 100044, China

[c] Department of Chemical Sciences, University of Padua, Via Marzolo 1, 35131 Padova, Italy

[d] Departament d'Enginyeria Química, EEBE, Universitat Politècnica de Catalunya, C/ Eduard Maristany, 10–14, Ed. I2, 08019 Barcelona, Spain

ARTICLE INFO

Keywords:
Biomass
Electro-Fenton
Gas-diffusion electrode
Hydrogen peroxide electrosynthesis
Water treatment

ABSTRACT

The excessive cost, unsustainability or complex production of new highly selective electrocatalysts for H_2O_2 production, especially noble-metal-based ones, is prohibitive in the water treatment sector. To solve this conundrum, biomass-derived carbons with adequate textural properties were synthesized via agarose double-step pyrolysis followed by steam activation. A longer steam treatment enhanced the graphitization and porosity, even surpassing commercial carbon black. Steam treatment for 20 min yielded the greatest surface area (1248 $m^2\ g^{-1}$), enhanced the mesopore/micropore volume distribution and increased the activity ($E_{1/2}$ = 0.609 V) and yield of H_2O_2 (40%) as determined by RRDE. The upgraded textural properties had very positive impact on the ability of the corresponding gas-diffusion electrodes (GDEs) to accumulate H_2O_2, reaching Faradaic current efficiencies of ~95% at 30 min. Acidic solutions of β-blocker acebutolol were treated by photoelectro-Fenton (PEF) process in synthetic media with and without chloride. In urban wastewater, total drug disappearance was reached at 60 min with almost 50% mineralization after 360 min at only 10 mA cm^{-2}. Up to 14 degradation products were identified in the Cl^--containing medium.

1. Introduction

The homogeneous and heterogeneous catalytic decomposition of H_2O_2 promoted by dissolved and solid Fe-based species, respectively, via general Fenton's reaction (1) is the core of the electro-Fenton (EF) treatment of organic pollutants in water (Brillas et al., 2009; Martínez-Huitle et al., 2015; Huong Le et al., 2017; Moreira et al., 2017; Ganiyu et al., 2018b; Monteil et al., 2019). The EF process yields a range of reactive oxygen radicals, with $^{\bullet}OH$ as predominant oxidant due to its highly positive standard reduction potential (E^0 = +2.730 ± 0.017 V) (Armstrong et al., 2015). This makes the technology extremely effective, although it is mandatory to ensure the continuous conversion of the Fe (III) species generated in solution. This is feasible under photoelectro-Fenton (PEF) conditions, which involves the photo-irradiation of the liquid phase with UVA light, according to reaction (2) (Wen et al., 2019; Brillas, 2020; Ye et al., 2020a, 2020d).

$$Fe^{2+} + H_2O_2 \rightarrow [Fe(OH)]^{2+} + {}^{\bullet}OH \quad (1)$$

$$[Fe(OH)]^{2+} + h\nu \rightarrow Fe^{2+} + {}^{\bullet}OH \quad (2)$$

The superiority of EF and PEF as compared to a simpler process like electro-oxidation with electrogenerated H_2O_2 (EO-H_2O_2) in terms of degradation rate has been widely demonstrated (Coria et al., 2016: Vasconcelos et al., 2016; Ganiyu et al., 2018a; Yang et al., 2019; Ye et al., 2019a). Despite the absence of iron catalyst, hydroxyl radical is produced in EO-H_2O_2 as well, via reaction (3), but it is strictly confined to the anode surface or its vicinity. This tends to limit the oxidation

* Corresponding authors.
E-mail addresses: christian.durante@unipd.it (C. Durante), i.sires@ub.edu (I. Sirés).
[1] These authors contributed equally to this work.

https://doi.org/10.1016/j.jhazmat.2021.127005
Received 2 February 2021; Received in revised form 16 August 2021; Accepted 19 August 2021
Available online 22 August 2021
0304-3894/© 2021 The Author(s). Published by Elsevier B.V. This is an open access article under the CC BY-NC-ND license (http://creativecommons.org/licenses/by-nc-nd/4.0/).

power of this process, unless the treated solution contains electroactive anions that can be transformed into powerful oxidants, as exemplified in reaction (4) (Thiam et al., 2018; Espinoza et al., 2020).

$$M+H_2O \rightarrow M(^{\bullet}OH)+H^+ +e^- \quad (3)$$

$$M+2Cl^- \rightarrow M+Cl_{2(aq)}+2e^- \quad (4)$$

Recently, new materials and setups have been developed to enhance the efficiency of EF and PEF treatments of pharmaceutical residues in water (Yang et al., 2018, 2020; Hammouda et al., 2019; Olvera-Vargas et al., 2020; Ye et al., 2020b, 2020c). Water pollution by excreted pharmaceuticals in their unmetabolized form has become a major issue worldwide, since they exert dramatic effects like endocrine disruption, secondary poisoning and antibiotic resistance (Bagnis et al., 2018; Desbiolles et al., 2018). The management of such contaminants is not only a matter of concern in urban wastewater treatment facilities, but it also entails environmental liabilities for pharmaceutical companies due to stricter environmental regulations (Larsson, 2014). Acebutolol, a commonly used β-blocker, exemplifies the gradual environmental accumulation of partially metabolized pharmaceuticals (Godoy et al., 2015). Up to 60% of this drug is excreted in its parent form once administered (Bussy et al., 2012), thereby posing serious risks to living beings (Fraysse and Garric, 2005; Godoy et al., 2015). Hitherto, methods like ozonation (Benner et al., 2008), TiO_2 photocatalysis (Bensaadi et al., 2014), chlorination (Khalit and Tay, 2016) or EO (Bussy et al., 2012) have been applied to degrade acebutolol in aqueous medium, but PEF process has not been examined yet.

Our research groups are currently developing optimized reactors (Salmerón et al., 2019; Ye et al., 2020a), suspended heterogeneous catalysts (Ye et al., 2020b, 2020c, 2020d) and cathode materials (Favaro et al., 2015a, 2015b; Perazzolo et al., 2016a, 2016b; Daniel et al., 2018; Brandiele et al., 2019; Ye et al., 2019b; Alcaide et al., 2020), aiming at serving for future scale-up of EF and PEF systems. Among the different cathode configurations, gas-diffusion electrodes (GDEs) are inspiring new catalytic routes (Shi et al., 2021), and those made with (Co, S, P)-decorated carbon nanotubes enhanced the electrocatalytic H_2O_2 production via 2-electron oxygen reduction reaction (5). This finding agrees with recent trends, since highly selective and active single metal atoms/catalysts (Pizzutilo et al., 2017; Wang et al., 2020) and polyatomic metal catalysts (Jirkovský et al., 2012) are especially targeted for enhanced H_2O_2 electrosynthesis.

$$O_2+2H^+ +2e^- \rightarrow H_2O_2 \quad (5)$$

In contrast, for wastewater treatment applications, there is need for carbonaceous GDEs that are as simple, cheap and sustainable as possible, preferably without any additional catalyst loading in order to simplify the manufacture, reduce the cost and prevent metal leaching that causes secondary pollution and lack of reproducibility (Favaro et al., 2015a; Perazzolo et al., 2015, 2016a, 2016b; Dong et al., 2020). This is especially critical when actual wastewater is treated, since natural organic matter (NOM) and inorganic ions can induce the fouling of the metallic sites of the electrocatalyst due to adsorption and precipitation phenomena, similarly to that observed in suspended catalysts (Ye et al., 2020b).

Metal-free carbon black is the most widespread carbon electrocatalyst for electrochemical water treatment (Dong et al., 2020; Xu et al., 2020), also in the case of GDEs (Coria et al., 2016; Lanzalaco et al., 2017; Ye et al., 2020a; Zhang et al., 2020). Nevertheless, this substrate is synthesized by incomplete combustion of hydrocarbons at high temperature (Zhang et al., 2019), thus being considered a dirty source. Within this context, we are particularly interested in greener and more economical carbon resources. Focus is put on the development of carbon powders derived from abundant biomasses, to be employed in the preparation of GDEs that generate H_2O_2 to sustain the Fenton's reaction (1). In accordance to new policies on the promotion of circular economy to foster the zero waste discharge, many authors have reported the preparation of biomass-derived carbons for oxygen reduction. New resources include carbohydrates and polysaccharides, as well as lignocellulose and animal biomass (Borghei et al., 2018). On some occasions, the selectivity of such carbons toward H_2O_2 electrosynthesis via reaction (5) has been assessed (Yang et al., 2017; Daniel et al., 2018; Tian et al., 2019; Jia et al., 2020). However, as far as we know, only a couple of studies have described their implementation in a GDE: Liao et al. (2019) reported the oxidation of formaldehyde by electrosynthesized H_2O_2, whereas the performance of EF and PEF with this type of GDE but using chitosan has only been tested in one of our most recent articles (Daniel et al., 2020).

This work addresses a doubly eco-friendly approach in the field of water treatment: H_2O_2 is produced on site upon modulation of applied current, avoiding the risks and costs associated to manipulation of commercial H_2O_2 and relying on a biomass-derived electrocatalyst. Refined agarose, a subfraction of a mixture of polysaccharides (i.e., agar) extracted from *Rhodophyta* marine red algae (seaweed) cells (Vadodariya et al., 2018), has been selected as an abundant and sustainable low-cost carbon biopolymer. The closest study was reported by Liu et al. (2016), who directly tested carbonized spiral seaweeds for oxygen reduction. Here, GDEs were prepared from agarose-derived carbons with different textural properties. Varying area and pore distribution, which determine the activity of carbon electrocatalysts, were conferred upon change of the synthesis conditions. The ordered structure of the resulting mesoporous carbons contributed to limit the residence of the generated H_2O_2 in the cathode vicinity, thus minimizing its destruction (Perazzolo et al., 2015, 2016a). The materials were fully characterized and the ability of the GDEs to produce H_2O_2 was tested at constant current density. Acebutolol was treated as the target pollutant by EF and PEF in various electrolytes, and the viability of the new electrocatalysts was validated in actual wastewater, also identifying the main reaction products.

2. Materials and methods

2.1. Chemicals

Agarose (CAS No. 9012–36–6, $SO_4^{2-} \leq 0.15\%$), purchased from Sigma-Aldrich and used as received, was the only reagent needed for the synthesis of the powdery catalysts. After their obtention, each selected powder was mixed with ethanol (96%, Panreac) and polytetrafluoroethylene (PTFE, 60 wt% solution, Sigma-Aldrich), to manufacture a GDE as described below. The ability of such GDEs to electrogenerate H_2O_2 was quantified upon reaction with $TiOSO_4 \bullet xH_2O$ (technical grade, Sigma-Aldrich). Acebutolol was from Sigma-Aldrich (hydrochloride salt, CAS number 34381–68–5) and its concentration was evaluated chromatographically using acetonitrile (high performance liquid chromatography (HPLC) grade) and KH_2PO_4 in the eluent, whereas the organic reaction products were extracted with CH_2Cl_2, all of them from Panreac. As discussed later, the main accumulated inorganic ion was ammonium, whose content was determined upon reaction with phenol (99.5%, Sigma-Aldrich), hydrated sodium nitroprusside ($Na_2[Fe(CN)_5NO] \bullet 2H_2O$, Merck) and hydrated ethylenediaminetetraacetic acid disodium salt (Na_2-EDTA, 99%, Alfa Aesar). Tris(hydroxymethyl)aminomethane ($\geq$ 99.8%) and phthalic acid ($\geq$ 99.5%), ACS reagents from Sigma-Aldrich, were employed in the ion chromatography analysis. *N,N*-Diethyl-*p*-phenylenediamine sulfate salt ($\geq$ 99%, Merck) was used for active chlorine quantification.

Ultrapure water ($\rho > 18.2$ MΩ cm at 25 ºC, pH ~5.5) obtained from a Merck Millipore Milli-Q system was employed for the preparation of the catalysts, GDEs and analytical solutions. Most of the electrolytic trials were carried out in such ultrapure water, in the presence of anhydrous Na_2SO_4 (Merck) and/or NaCl (Panreac) as background electrolytes. For validation, some degradation trials were also made in the secondary effluent from a municipal wastewater treatment plant as actual water

matrix. It had a pH of 7.5, specific conductivity of 2.1 mS cm^{-1} and total organic carbon (TOC) of 10.4 mg L^{-1}. The cation and anion contents were determined according to a previous work (Ye et al., 2020a). This water sample was preserved at 4 ºC after acidification and homogenization to prevent bacterial growth. Prior to the electrolyses, the pH of all solutions was adjusted to pH 3.0 as optimal for Fenton's reaction (1) (Brillas et al., 2009; Martínez-Huitle et al., 2015), using analytical grade H_2SO_4 (96%) or HCl (37%) from Merck. $FeSO_4$•$7H_2O$ (Panreac) was the catalyst source in EF and PEF.

2.2. Synthesis of agarose-derived catalysts

To synthesize mesoporous carbons from agarose (so-called MCA), an agarose hydrogel was pyrolyzed following a procedure previously described in detail (Daniel et al., 2018). Agarose is a green, highly disposable and non-toxic chemical. Moreover, it has a fast gelation rate and yields a stable gel with interconnected pores, an architecture that can be transferred to the carbon obtained upon pyrolysis. The agarose hydrogel was prepared by dissolving 2 g of agarose in 25 mL of milli-Q water, and the resulting mixture was heated to boiling and then cooled down to room temperature to form a stable hydrogel. The gel was then chopped up into small pieces to ease the removal of water by freeze-drying for preserving the porous structure. The dried hydrogel was pyrolyzed according to a two-step sequence (each step for 2 h), at 400 °C and 900 °C. This was made in a tubular furnace (Carbolite) using a 75 sccm (i.e., standard cm^3 min^{-1}) N_2 flux and a heating ramp of 5 °C min^{-1}. The crude product obtained after the first heating step (so-called MCA@400), as well as the final carbon (MCA@900), were ground by vibro-milling (Retsch MM 400, four steps of 4 min at 10–25 Hz). The effect of a novel post-treatment on the textural properties and performance was also investigated. For this, the resulting MCA was further activated in steam at 850 °C under N_2 flux of 50 sccm. The setup for the steam treatment consisted in a tubular furnace flanged at both sides to control the inner atmosphere. The outlet flange was connected to the purging line directed to a scrubber, whereas the inlet flange was connected to the N_2 mass flow control. The inlet flange also lodged a stainless steel needle, which was connected to a syringe pump and positioned so that the needle tip laid at the entrance of the oven. The syringe pump was actioned after purging the tubular furnace with N_2 and once the temperature reached 850 °C. The syringe pump injected milli-Q water at 1 mL min^{-1} right in the front entrance of the tubular furnace, achieving the almost instantaneous water evaporation. The MCA@900 samples were exposed to the steam treatment during different time periods, 5, 10 and 20 min, giving rise to three types of carbons: MCA@900_5, MCA@900_10 and MCA@900_20. These names are used throughout the manuscript, as compared to the sample not exposed to the steam treatment (MCA@900).

2.3. Physicochemical characterization of agarose-derived catalysts

Transmission electron microscopy (TEM) images were acquired with a FEI Tecnai G2 transmission electron microscope that was operated at 100 kV. For Brunauer-Emmett-Teller (BET) analysis, isotherm and pore distribution, nitrogen adsorption-desorption was carried out at 77 K employing a Micromeritics ASAP2020. The surface area values were obtained from the desorption curve in a multipoint BET analysis and the pore distribution was assessed with a slit/cylindrical pore QSDFT (i.e., quenched solid density functional theory) non-equilibrium model. The elemental analysis (EA) was performed in a Thermo Scientific Flash 2000 instrument. Fourier transform infrared spectroscopy (FTIR) was employed to evaluate the surface functionalities. The spectra were recorded on a Bruker Vertex 70 FTIR spectrometer, equipped with a diamond ATR device (Golden Gate, Bruker) to operate in transmission mode. Samples were prepared by mixing powders (1 wt%) in KBr. X-ray photoemission spectroscopy (XPS) measurements were performed at room temperature in a UHV chamber (base pressure $< 5 \times 10^{-9}$ mbar), equipped with a double anode X-ray source (Omicron DAR-400) and a hemispherical electron analyzer (Omicron EIS-125). A non-monochromatized Mg-Kα radiation ($h\nu$ = 1253.6 eV) and pass energies of 50 and 20 eV for the survey and the single spectral windows, respectively, were used. The calibration of the Binding Energy (B.E.) was made using Au $4f_{7/2}$ as the reference (B.E. Au 4 $f_{7/2}$ = 84.0 eV). The XPS signal of carbon was deconvoluted into single components by using symmetrical Voigt functions. XRD measurements were made on a D8 ADVANCE Bruker diffractometer equipped with a Cu anode X-ray tube (40 kV, 40 mA), Bragg–Brentano HD optical module, and X'Celerator detector. Diffraction patterns were acquired in the 10–60º 2θ range with 0.01º virtual step size, counting an equivalent time of 0.5 s per step. The experimental diffractograms were compared with the standard ones (Powder Diffraction File database) to individuate the phases. Raman scattering analysis was conducted on a Thermo Scientific DXR Raman microscope system, equipped with a 532 nm laser as the photoexcitation source. The size of the laser spot at the sample was about 25 μm and the power at the sample was 1.0 mW. Curve fitting of the Raman spectra was made using Gaussian curves. Because of low S/N ratio, first- and second-order spectra were fitted separately by constraining the range of spectral parameters in the iteration procedure.

2.4. Electrolytic trials

Different electrolytic runs were conducted in order to assess the ability of the EO-H_2O_2, EF and PEF processes to electrogenerate H_2O_2 and active chlorine, as well as to compare the degradation rate of the selected pharmaceutical pollutant and identify the main products. A single compartment glass cell was chosen to carry out the experiments, allowing the co-generation of powerful oxidants from cathodic and anodic reactions. The cell always contained 150 mL of solution volume (V_s), which was prepared with ultrapure water or actual wastewater, acidified to pH 3.0, thermostated at 25 ºC and continuously stirred with a magnetic bar at 700 rpm. In most trials, acebutolol was spiked into the aqueous matrix, always at a concentration of 0.046 mM (10 mg L^{-1} TOC). EF and PEF treatments were made in the presence of 0.50 mM Fe^{2+} as catalyst. In PEF, the solution was irradiated with UVA light using a 6 W Philips lamp (tubular shape, λ_{max} = 360 nm, irradiance of 5 W m^{-2}) placed at 5 cm over the liquid surface.

In all these trials, the cell contained a RuO_2-based anode (dimensionally stable electrode, DSA-Cl_2) from NMT Electrodes placed in parallel to a GDE that served as the cathode. A GDE was prepared from each type of synthesized MCA catalyst using the air-brushing method (Ye et al., 2019b; Alcaide et al., 2020). To do this, 0.1 g of a given MCA powder were dispersed in a PTFE + ethanol mixture for 45 min using an ultrasonic bath, thus obtaining a volume of about 20 mL. The resulting ink was sprayed over a piece of ~8 cm^2 of degreased carbon cloth (BASF B1ASWP) employing a gun fed with N_2 gas. Several layers were applied, allowing the drying of each one at 60 ºC for 3 min, until the ink was finished. The final coated sample was pressed at 2 tons for 45 s, further annealed at 400 °C for 1 h under N_2 atmosphere and finally cooled down at room temperature. The weight gain in each GDE was about 80 mg (i.e., MCA-PTFE loading of 9.7 mg cm^{-2}). This coated carbon cloth was placed at the bottom of a tubular polypropylene housing, which acted as a gas chamber fed with compressed air pumped at 0.6 L min^{-1} to ensure a continuous H_2O_2 electrogeneration. The geometric area of both electrodes was 3 cm^2 and the interelectrode gap was 1 cm. Constant current between the anode and cathode was supplied by an Amel 2051 potentiostat-galvanostat, and a Demestres 605 multimeter monitored the cell voltage (E_{cell}). The E_{cell} values ranged between 3.6 and 4.0, 6.9–7.4 and 12.5–13.0 V at 10, 30 and 60 mA cm^{-2}, respectively. Before first use of the new GDEs, their surface was conditioned and stabilized through a galvanostatic polarization made in a 0.050 M Na_2SO_4 solution, at 300 mA for 180 min.

2.5. Analytical methods

The solution pH was monitored upon initial adjustment to 3.0 and during the electrolyses using a Crison GLP 22 pH-meter. A Metrohm 644 conductometer was employed for conductivity measurements. Before each of the following analyses, the samples were pre-conditioned by filtration with PTFE filters (13 mm × 0.45 μm) from Whatman. The colorimetric analysis of the yellowish complex formed between Ti(IV) and H_2O_2 was made at 25 ºC on a Unicam UV/Vis spectrophotometer set at $\lambda_{max} = 408$ nm (Welcher, 1975). The corresponding calibration curve equation, Absorbance = 0.0351 [H_2O_2] (with [H_2O_2] in mM), allowed the determination of the current efficiency (CE) over the time, as follows (Brillas et al., 2009):

$$\mathrm{CE\ (in\ \%)} = \frac{2F[\mathrm{H_2O_2}]V_s}{M(\mathrm{H_2O_2})Q}100 \quad (6)$$

where 2 is the number of electrons transferred for H_2O_2 production according to reaction (5), F is the Faraday's constant, [H_2O_2] is in g L^{-1}, V_s is in L, $M(H_2O_2)$ is the molecular weight of the oxidant in g mol^{-1} and Q is the charge consumed during the electrolysis in C.

The same instrument was employed to determine the concentrations of active chlorine, at $\lambda_{max} = 515$ nm (APWA et al., 2005) and NH_4^+ ion, at $\lambda_{max} = 630$ nm (Ye et al., 2019b). The drug concentration decay over time was measured by reversed-phase HPLC. A Waters 600 chromatograph, equipped with a BDS Hypersil C18 column thermostated at 35 ºC and connected to a photodiode array detector, was employed. A thin peak with $\lambda_{max} = 235$ nm related to acebutolol appeared at retention time of 4.6 min. A 40:60 (v/v) mixture containing the organic (acetonitrile) and aqueous (10 mM KH_2PO_4 solution at pH 3.0) phases, respectively, was recirculated at 1.0 mL min^{-1} as mobile phase. The degradation trials were made twice and average drug concentration values along with their error bars (95% confidence interval) are depicted in the figures. Short-chain carboxylic acids were quantified using the same instrument, although equipped with a Bio-Rad Aminex column and replacing the previous mobile phase by a 4 mM H_2SO_4 solution at 0.6 mL min^{-1} (Coria et al., 2016). The detection was made at $\lambda_{max} = 210$ nm, with peaks for oxalic and maleic acids at 7.0 and 8.5 min. The inorganic anions in raw wastewater were quantified as described before (Ye et al., 2020a), with a Shimadzu 10Avp chromatograph coupled to a conductivity detector.

The solution TOC was determined by injecting the samples in a Shimadzu TOC-VCNS analyzer and selecting the non-purgeable organic carbon (NPOC) method. From the TOC value of each aliquot, with ± 1% accuracy, $\Delta(\mathrm{TOC})_{exp}$ was calculated in mg L^{-1} and the mineralization current efficiency (MCE) was calculated as follows (Thiam et al., 2018):

$$\mathrm{MCE\ (in\ \%)} = \frac{nFV_s(\Delta\mathrm{TOC})_{exp}}{4.32x10^7 mIt}100 \quad (7)$$

considering the applied current I, in A, and a given electrolysis time t, in h. The number of carbon atoms of acebutolol molecules (m) and the number of electrons involved in their mineralization (n) are shown in the overall mineralization reaction:

$$C_{18}H_{28}N_2O_4 + 32H_2O \rightarrow 18CO_2 + 2NH_4^+ + 84H^+ + 86e^- \quad (8)$$

The specific electrolytic energy consumption per unit TOC mass (EC_{TOC}), which accounts for the energy required to run the electrochemical process, was obtained as follows (Thiam et al., 2018):

$$\mathrm{EC_{TOC}\ (in} kWh(\mathrm{g\ TOC})^{-1}) = \frac{E_{cell}It}{V_s(\Delta\mathrm{TOC})_{exp}} \quad (9)$$

where E_{cell} is the average value, in V.

Gas chromatography-mass spectrometry (GC/MS) analysis allowed the identification of the organic products generated during drug degradation. They were extracted with CH_2Cl_2 as organic solvent, whereas their analysis was made in electron impact mode at a voltage of 70 eV using an Agilent Technologies instrument composed of a 6890 N chromatograph linked to a 5975 mass spectrometer. Teknokroma Sapiens-X5.ms (non-polar) and HP-INNOWax (polar) columns (0.25 μm, 30 m × 0.25 mm (i.d.)) were employed. The method followed in each case is detailed elsewhere (Ye at al., 2020c), with 67.80 and 93.80 min as run time, respectively. For a correct interpretation, the mass spectra were compared to those found in the NIST05 MS database.

The agarose-derived electrocatalysts were characterized by cyclic voltammetry (CV) and linear sweep voltammetry (LSV) at a rotating ring-disk electrode (RRDE from Metrohm containing a 5 mm diameter glassy carbon disk surrounded by a Pt ring with a collection efficiency of 25%), in either Ar-purged or O_2-saturated 0.0005 M H_2SO_4 + 0.050 M Na_2SO_4 solutions using a 101 N Autolab potentiostat-galvanostat. The measurements were made in a three-electrode cell that included the RRDE as working electrode, alongside a graphite rod and a reversible hydrogen electrode (RHE) as the counter and reference electrodes, respectively, at a scan rate of 5 mV s^{-1} and a rotation speed (ω) of 1600 rpm. The electrocatalysts were characterized as thin films prepared as an ink by drop-casting (20 μL) of the corresponding carbon powder on the disk. All the electrochemical assays were carried out with an optimized loading of 0.6 mg cm^{-2}. The number of electrons transferred during ORR (n) and the H_2O_2 yield ($y_{H_2O_2}$) were determined according to reported equations (Daniel et al., 2020), after measuring the disk and ring currents (I_D and I_R, respectively) and considering a collection efficiency (N) of 0.25.

The GDEs prepared with agarose-derived carbon catalysts (both fresh and used) were characterized by scanning electron microscopy (SEM) employing a JSM-7100F field emission microscope from JEOL at 20.0 kV.

3. Results and discussion

3.1. Characterization of the synthesized MCA catalysts

Fig. 1 collects the TEM images of each of the MCA materials obtained, at two different magnifications. MCA@400, which is the product of the first pyrolysis step at 400 °C, is composed of foam-like graphitic sheets that apparently did not present a defined pore structure (Fig. 1a and b). After the second pyrolysis step, the resulting MCA@900 maintained a compact structure, even though open alveoli-like features could be distinguished (Fig. 1c and d). The effect of the steam treatment on compactness is clearly visible in the other images. As steam was applied for a longer time of 5 min (MCA@900_5, Fig. 1e and f), 10 min (MCA@900_10, Fig. 1g and h) and 20 min (MCA@900_20, Fig. 1i and j), the initially dense structure of MCA@ 900 left space to voids and carbon slag, resulting in an interconnected disordered hierarchical pore structure. Such less packed structure promoted by steam is presumed to be positive, favoring the transport of reactants. Among those, the promoted contact of protons and organic molecules with the electrocatalyst surface enhances, respectively, the production of H_2O_2 from reaction (5) and the reactive events with $^{\bullet}OH$ formed via reaction (1).

The EA data of the agarose-derived carbons are summarized in Table 1. The direct analysis evidenced the presence of carbon and hydrogen, the remaining percentage being tentatively assigned to oxygen because no other impurities were found. As it can be observed, the percentage of oxygen, and therefore the number of oxygen functionalities bounded to the carbon support, increased when moving from MCA@900 to MCA@900_10. In contrast, it tended to decrease as the steam treatment was prolonged. This behavior is consistent with a milder oxidation of the most reactive carbon atoms upon short steaming, whereas a longer exposure induced the release of CO or CO_2 gases. It is worth noting that these gases played a fundamental role as porogen agents, becoming beneficial to enhance the textural properties of the support.

Aiming to complement the EA results, the functionalities induced on

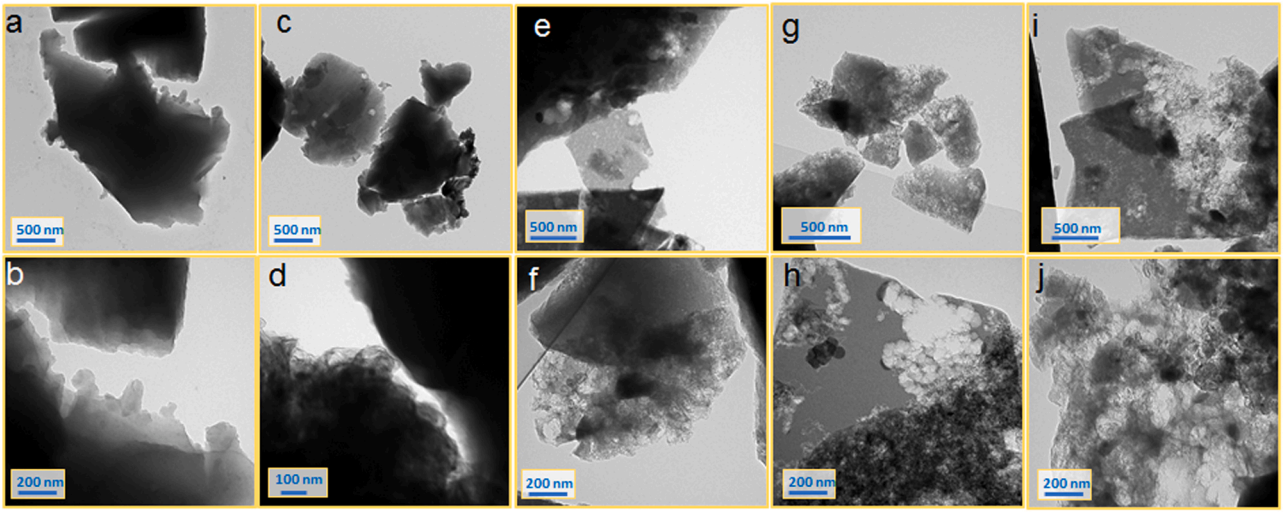

Fig. 1. TEM images obtained at (a,c,e,g,i) lower and (b,d,f,h,j) higher magnification: (a,b) MCA@400 catalyst, resulting from the first step of pyrolysis, (c,d) MCA@900 catalyst, produced after the second step of pyrolysis, and catalysts obtained upon steam treatment of MCA@900 powder for (e,f) 5 min (MCA@900_5), (g, h) 10 min (MCA@900_10) and (i,j) 20 min (MCA@900_20).

Table 1
Elemental analysis (EA) and analysis of N_2 adsorption/desorption data based on the QSDFT model for MCA@900 catalysts, non-activated and activated for 5, 10 and 20 min.

Catalyst	EA			QSDFT (slit/cylindrical) adsorption model[a]							
	C (%)	H (%)	O (%)[b]	S_{QSDFT} ($m^2\ g^{-1}$)	S_{μ} ($m^2\ g^{-1}$)	S_m ($m^2\ g^{-1}$)	V_{TOT} ($cm^3\ g^{-1}$)	V_{QSDFT} ($cm^3\ g^{-1}$)	V_{μ} ($cm^3\ g^{-1}$)	V_m ($cm^3\ g^{-1}$)	HF
MCA@900	85.93	0.76	13.31	487	477	10	0.195	0.173	0.156	0.017	0.02
MCA@900_5	67.43	0.62	31.95	908	873	35	0.324	0.292	0.249	0.043	0.03
MCA@900_10	65.72	0.53	33.75	992	926	66	0.440	0.392	0.289	0.103	0.04
MCA@900_20	81.31	0.59	18.10	1248	1040	208	0.854	0.724	0.379	0.345	0.07

[a] QSDFT: Quenched solid density functional theory.
[b] Oxygen content determined by difference from (C + H) content in EA.

MCA@900 sample by the steam treatment were analyzed from FTIR spectra, which were normalized considering the peak centered at ~2920 cm^{-1} assigned to the stretching vibration of the aliphatic C–H bonds of the agarose hydrogel used as precursor. As shown in Fig. 2, the typical peak located at 3430 cm^{-1} arises from the O–H stretching vibration stemming from water, whereas the three peaks at 2970, 2920 and 2850 cm^{-1} are related to the stretching vibration of the C–H bonds (Singh et al., 2017). The sharp absorption peaks observed at 1670 and

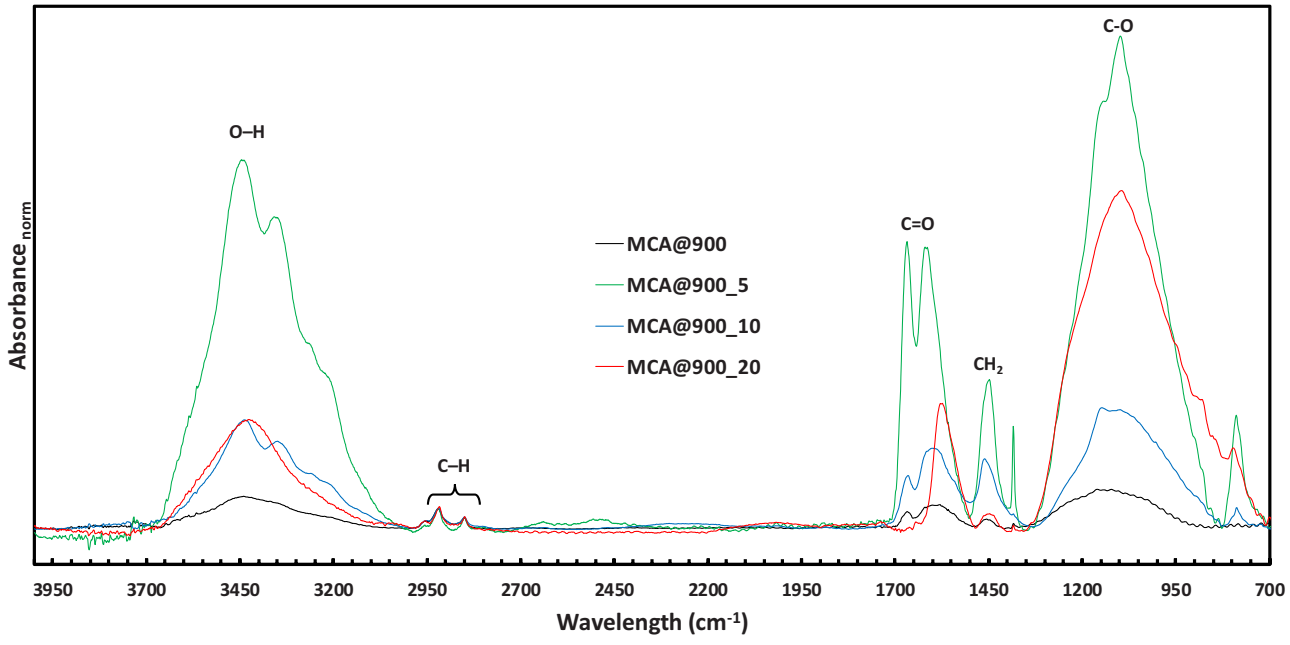

Fig. 2. FTIR spectra for all the MCA@900 catalysts, non-activated and activated for 5, 10 and 20 min.

1620 cm^{-1} are assigned to the stretching vibration of groups that contain the C═O functionality, while the distinct peak at 1465 cm^{-1} is attributed to the C–H vibration mode of the CH_2 groups (Yang et al., 2016). Finally, the other peaks centered at 1345 and 1050 cm^{-1} correspond to the C–O stretching vibration (Yang et al., 2016). As compared to the non-activated carbon, all the samples that underwent the steam treatment presented a higher absorbance of the peaks related to oxygenated functional groups (Fig. 2), thus confirming the EA results. Since the spectra are normalized considering the C–H vibrations, the changes observed can be explained from the relative amount of C and O in each sample. More in detail, the steam process seems to favor the presence of the C═O and C-O groups especially after 5 min of treatment. A longer exposure caused their decrease but not their disappearance and hence, the presence of such oxygen functionalities in all the treated samples is expected to have a very positive impact, as the adjacent carbons act as active sites for H_2O_2 production (Lu et al., 2018). These findings allow corroborating that the steam treatment affects the molecular structure of the material and the available functional groups, with a consequent direct impact on the textural properties, resistance and electroactivity.

The FTIR results were corroborated by means of XPS analysis, which revealed the presence of the sole C 1*s* and O 1*s* signals. The latter are not really informative because of a persistent environment contamination from atmospheric oxygen, in contrast to C 1*s* that can give some clues about the evolution of the carbon environment during the steam treatment. In Fig. S1a in Supplementary Material, only the spectra of the untreated and the MCA@900_20 samples are shown, since in all cases they were superimposable, with the exception at high binding energy where the MCA@900_20 spectrum slightly differs in a higher concentration of the $\pi \rightarrow \pi^*$ transition, which is typical of polyoxygenated groups. The presence of the different oxygen functionalities, which agrees with FTIR results, is shown in Fig. S1b and c.

In order to quantify the change of the textural properties of the synthesized carbons, their hierarchical pore structure and surface area were evaluated by N_2 physisorption at 77 K (Fig. 3). MCA@900 presented a Type-I(a) isotherm with a horizontal plateau, which is typical of a microporous material mainly composed of ultramicropores (pore diameter < 0.7 nm). The filling of micropores is a continuous process, which can be observed at low P/P^0 values (Fig. 3a), being governed by the enhanced gas-solid interactions (Cychosz et al., 2017). The analysis of this kind of materials is performed using an advanced method like QSDFT, which takes into account the surface roughness, the filling mechanism of micropores and the mechanism of pore condensation, evaporation and hysteresis. The uptake limit was constrained by the accessible micropore volume rather than by the internal surface area. As can be seen, for the MCA@ 900 sample, the adsorption and desorption branches were not overlapped, a behavior that is probably due to the pore shape. The pore morphology could block the outgassing, thus requiring a higher equilibration delay during desorption. The prevalent microporosity of MCA@ 900 can be confirmed from Table 1, as the QSDFT analysis revealed micropore surface (S_μ) and volume (V_μ) values much greater than mesopore ones (S_m and V_m). The same type of isotherm was maintained for the steam-treated samples, with the exception that in MCA@ 900 the hysteresis loop was missing. Such loop was Type H4 in MCA@900_5 and MCA@ 900_10, which is typical of micro-mesoporous materials. In fact, the steam treatment gradually induced: (i) the formation of bigger pores (i.e., greater S_m/S_μ and V_m/V_μ ratios, Table 1), and (ii) the consequent enhancement of the pore volume (Fig. 3b) and the surface area (Table 1) from 487 $m^2\ g^{-1}$ (MCA@900) to 1248 $m^2\ g^{-1}$ (MCA@900_20). The latter is comparable to the value reported for carbons prepared from magnolia flowers, with a surface area of 1226 $m^2\ g^{-1}$ (Chen et al., 2017), and slightly greater than the BET surface area of a nanoporous electrocatalyst synthesized from pomelo peel (i.e., 1106 $m^2\ g^{-1}$) (Yang et al., 2017). It is worth mentioning that the area of our agarose-derived catalysts is much greater than that achieved by Garza-Campos et al. (2018). These authors prepared mesoporous carbons from formaldehyde/resorcinol mixtures by a soft template method followed by carbonization and then tested them in GDEs for water treatment. Their surface area ranged from 476 to 646 $m^2\ g^{-1}$ and the maximum pore volume was 0.509 $cm^3\ g^{-1}$, which is much lower than that of MCA@900_20 (Table 1). All of the MCA samples synthesized here can be classified as carbons with high porosity and good textural properties, largely upgrading those of commercial carbon black (S_{BET} = 67 $m^2\ g^{-1}$, V_μ = 0.015 $cm^3\ g^{-1}$, V_{meso} = 0.137 $cm^3\ g^{-1}$) typically employed to prepare GDEs for water treatment.

In MCA@900_5 and MCA@900_10 isotherms, the desorption close to P/P^0 of 0.45 (Fig. 3a) can be explained by the cavitation effect induced by ink-bottle shape of pores. Fig. S2 shows the pore size distributions centered at 0.9, 2.3 and 5 nm for MCA@900, MCA@900_5 and MCA@900_10, respectively. A quite different adsorption/desorption behavior can be recognized for MCA@900_20, which is characterized by a Type H3 hysteresis loop. In fact, in this case the pore size distribution depicted in Fig. S2 is much broader, ranging from 2 to 20 nm. The enlarged mesopore neck size favored the outgassing, obtaining a more defined and closed hysteresis loop with no cavitation effect.

From the catalytic point of view, accessibility and connectivity between pores is fundamental. A dimensionless hierarchical factor (HF = $[(V_\mu/V_T) \times (S_m/S_{QSDFT})]$), which is typically employed to evaluate the catalytic activity of zeolites, was calculated to correlate structure with catalytic performance. As summarized in Table 1, the HF increased at longer steam treatment, attaining a maximum value for the MCA@900_20 sample. This is explained by the greater increase of mesoporosity as compared to microporosity (Pérez-Ramírez et al., 2009), which corroborates that steam promoted the creation of new mesopores and the size increase of existing pores.

Note that the transition from micro to mesopores as the steam treatment became longer, reaching a V_m/V_μ ratio near 1 for MCA@900_20, is a remarkable property because of the combined benefits of both types of pores. Microporosity is positive because of the high

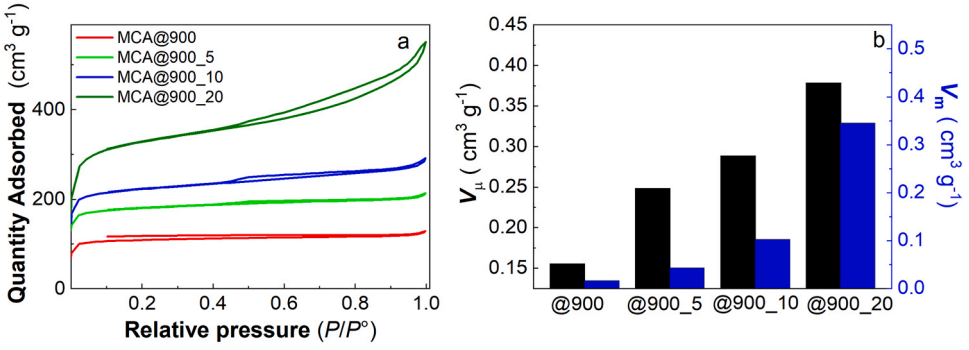

Fig. 3. (a) Nitrogen adsorption/desorption isotherms for all the MCA@900 catalysts described in Fig. 2. (b) Effect of steam treatment on the micro/mesopore volume (V_μ and V_m, respectively).

internal surface area of pores and their ability to bind gases like O_2, as shown for polymers of intrinsic microporosity (Madrid et al., 2019), whereas mesoporosity is associated to a favorable mass transport with lower resistance (Qin et al., 2020). An excess of micropores with small openings hinders the mass transport, restricting the formation of the three-phase boundary (Lee et al., 2019), but a sufficient amount is needed to provide a good number of active sites (Jaouen et al., 2006). Therefore, these pores must be adequately combined with mesopores to ensure the continuous reactivity (access of reagents and exit of products, both in the ORR to H_2O_2 and in the pollutant degradation).

Raman spectroscopy gives insightful information on carbon materials since it is sensitive not only to crystals but also to molecular structures (i.e., short-range order) (Sadezky et al., 2005), providing valuable information on the graphitization degree. The Raman spectra of Fig. 4a show a clear evolution upon steam treatment. The two most evident bands, at ~1350 and ~1600 cm^{-1}, are respectively called D1 and G bands in analogy to the Raman features of graphite (Brandiele et al., 2019). The D1 band is related to the disordered graphitic lattice on the edges of graphene layers, whereas the G band describes the vibration of the sp^2 sites on an ideal graphitic lattice. Some earlier studies suggested that the peak at ~1600 cm^{-1} can be deconvoluted into two bands, G and D2, the latter arising from the disordered graphitic lattice on the surface of graphene layers (Brandiele et al., 2019). To fit the experimental data, the inclusion of the D2 band is clearly necessary mostly on non-activated carbons, such as MCA@ 900 and MCA@900_5 (see Raman data deconvolution for this sample in Fig. 4b). Between D1 and G bands, another band (D3) can be assigned at ~1500 cm^{-1}, accounting for amorphous carbon (Perazzolo et al., 2015). According to several studies, a Gaussian fitting was proposed for D3 band due to a statistical distribution of amorphous carbon in interstitial positions of the disturbed graphitic lattice (Javhori et al., 1995). The band at ~1350 cm^{-1} seems to exhibit a shoulder at ~1220 cm^{-1}, which can be deconvoluted to yield a D4 band attributed to sp^2-sp^3 bonds or C−C and C═C stretching vibrations (Sadezky et al., 2005). D3 and D4 bands are usually present in highly defective carbon (Bokobza et al., 2015). The parameters obtained from spectra fitting (Table S1 in Supplementary Material) allow analyzing the amorphous carbon using a phenomenological three-stage model. Different factors affected the shape of the spectra, and an amorphous trajectory can be defined considering the D1/G ratio and G band position (Brandiele et al., 2019). As summarized in Table S1, the G band shifted between 1593 and ~1598 cm^{-1}, whereas D1/G increased from 1.27 up to 1.78. Considering the Tuinstra-Koenig model, the band intensity ratio allowed the determination of the size of the graphite nanocrystallites, which was within the range 2.8–3.9 nm. The evolution of the two Raman parameters suggests that catalysts synthesized at 900 ºC can be classified in the first stage on the amorphization trajectory, from graphite to nanocrystalline graphite (Ferrari and Robertson, 2000). Also, the parameter R2, calculated from the areas of several bands as D1/(G + D1 + D2) (Beyssac et al., 2003), can reliably distinguish poorly (R2 > 0.5) and highly (R2 < 0.5) graphitized carbons. MCA@900 had the lowest R2, accounting for a high graphitization degree (Table S1). A short steam treatment for 5 min yielded a significantly lower graphitization (R2 = 0.60). This agrees with TEM and N_2 adsorption/desorption analyses, since steam induced a greater porosity increasing the disorder of the carbon lattice. However, a longer steam treatment favored graphitization (R2 = 0.54), which is related to a reduction of amorphous carbon (see decrease of D3 band in Fig. 4a and Table S1). The highest graphitization of MCA@900_20 is beneficial since it entails a greater conductivity, which promotes a better current distribution in the corresponding GDEs.

The second order Raman signals (2400–3200 cm^{-1}) were broad and overlapped (Fig. 4a). By prolonging the steam treatment, the profile became more defined, and the resulting bands could be attributed to overtones and a combination of vibration modes (Fig. 4b). Two bands, at ~2700 and ~2900 cm^{-1}, can be associated to 2*D1 overtone and a (D1 + G) combination, respectively (Daniel et al., 2018). No further information about the graphitization degree was obtained and stacking of graphene layers can be obtained from 2D1 and D1 + G bands due to the poor resolution (Bokobza et al., 2015).

The Raman analysis seems to inform quite clearly about the presence of amorphous carbon in all the samples. This was further confirmed by XRD analysis, which yielded similar diffraction patterns for all the materials, as exemplified in Fig. S3 for the untreated and MCA@900_20 samples. It is possible to observe only broad bands, with maxima at 2θ around 22.8º and 43.5º, which account for highly disordered graphite (0 0 2) and (1 0 1) reflections (JCPDS, Card No. 75–1621). Worth noting, there is a downward shift as compared to a perfectly crystallized graphite, which can be related to an expansion of the interlayer distance and small crystallite size, as confirmed by the increase of the full width at half maximum (FWHM) along with the decrease of the diffraction angles. It can then be said that the carbon remains in a form very similar to an amorphous carbon notwithstanding the steam treatment, which however allows the decrease of the background, eventually exalting the graphite reflections.

3.2. Ability of the agarose-derived GDEs to electrogenerate H_2O_2

The RRDE technique is widely employed to quantify the catalysts H_2O_2 activity and selectivity (Xia et al., 2020). In Fig. S4a and b, the ring and disk currents recorded for the four materials are depicted within the scanned potential range. Several relevant electrochemical parameters determined from these voltammograms are summarized in Table S2. Being $E_{1/2}$ and j_k good descriptors for the catalytic activity, it can be observed that even the shortest steam treatment (5 min) is able to cause a remarkable improvement in the electroactivity (as deduced from the much more positive $E_{1/2}$ and much greater j_k), which agrees with the almost 2-fold increase of S_μ (Table 1). Longer steam treatments did not exert such a significant impact on these parameters, although it is clear that the MCA@900_20 catalyst has the most positive $E_{1/2}$ and all the activated materials have an $E_{1/2}$ that is more positive than that

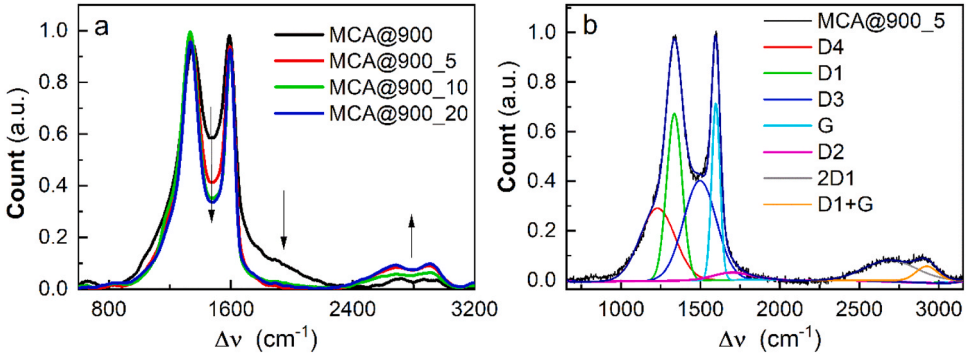

Fig. 4. (a) Experimental Raman spectra of all the MCA@900 catalysts described in Fig. 2. (b) Deconvolution of D and G spectral regions for the MCA@900_5 catalyst.

determined for chitosan-derived N-doped carbon ($E_{1/2}$ = 0.437 V) (Daniel et al., 2020). It is worth noting that the voltammetric curves of Fig. S4, especially those from the activated catalysts, show a two-step process, meaning that a first reduction yields H_2O_2 from O_2. The $y_{H_2O_2}$, defined by the ring current, finds its maximum at 0.6 V, attaining the highest value near 40% for the MCA@900_20 catalyst. Worth mentioning, this value is significantly better than 25% determined for chitosan-derived N-doped carbon (Daniel et al., 2020), which allows expecting a superior performance during bulk electrolysis (see below in this subsection).

To complete the previous results, single GDEs were subsequently prepared with each synthesized electrocatalyst in order to assess their ability to accumulate H_2O_2 in an undivided cell for 360 min under different conditions. Fig. 5a-d illustrate the evolution of the H_2O_2 concentration in 0.050 M Na_2SO_4 solutions at pH 3.0 using the MCA@900, MCA@900_5, MCA@900_10 and MCA@900_20 catalyst. First, one can realize that the electrogeneration was feasible with all the synthesized carbons. In the EO-H_2O_2 trials (i.e., without Fe^{2+}), which were carried out at three *j* values, a gradual accumulation of the oxidant with the electrolysis time can be observed. At each *j*, the profiles were linear during the first minutes. This can be explained by the predominance of the electrogeneration reaction (5), giving rise to the greater H_2O_2 accumulation despite its natural self-decomposition in the bulk and its partial destruction via cathodic reduction. Afterwards, the H_2O_2 concentrations tended to stabilize over time. The destruction rate of H_2O_2 in that stage, feasible in the undivided cell via anodic oxidation to yield $HO_2^{\bullet}$, progressively acquired more importance and could finally balance the cathodic production rate (Salmerón et al., 2019; Alcaide et al., 2020). The concentration *plateau* is more or less evident depending on the cathode material and the *j* value. For example, using the MCA@ 900 electrocatalyst (Fig. 5a), a gradually higher accumulation of 5.1, 14.0 and 20.3 mM was achieved at 360 min when *j* was increased from 10 to 30 and 60 mA cm^{-2}, respectively. This type of enhancement at greater *j*, arising from the acceleration of reaction (5), can also be observed for the other three electrocatalysts (Fig. 5b-d).

The accumulation of H_2O_2 is not a goal in itself in this work, because it is considered a mild oxidant against organic pollutants (Brillas et al., 2009). Therefore, its decomposition under EF conditions (i.e., in the presence of 0.50 mM Fe^{2+} as catalyst) was investigated at 10 mA cm^{-2}. Using the MCA@900 catalyst-derived GDE, the final accumulated H_2O_2 concentration was 2.4 mM (Fig. 5a), which is half of the above-mentioned value obtained in EO-H_2O_2. This remarkable decrease of about 50% can be seen for all catalysts (Fig. 5b-d), becoming a clear evidence of the occurrence of Fenton's reaction (1) and hence, of the $^{\bullet}OH$ production. Note that the amount of accumulated H_2O_2 in these EF systems agrees with the values reported in analogous setups in which a commercial GDE was employed (< 10 mM at 10–30 mA cm^{-2}) (Coria et al., 2016; Steter et al., 2016).

The reduction in the final H_2O_2 concentration was even more pronounced under PEF conditions (i.e., with 0.50 mM Fe^{2+} and solution

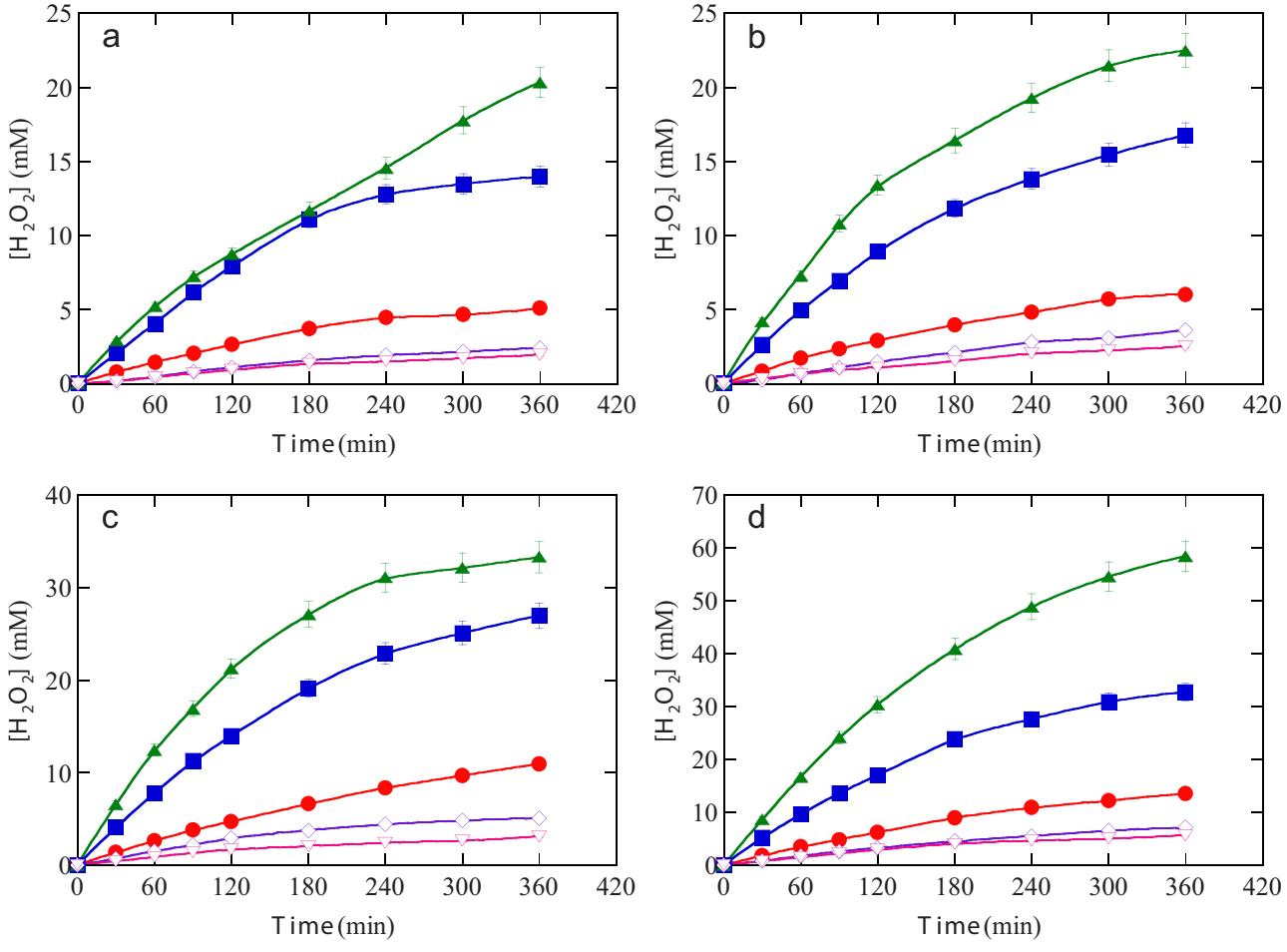

Fig. 5. Evolution of H_2O_2 concentration during the electrolysis of 150 mL of a 0.050 M Na_2SO_4 solution at pH 3.0 and 25 °C, using a cell with a RuO_2-based anode and a GDE as cathode prepared with (a) MCA@900, (b) MCA@900_5, (c) MCA@900_10 and (d) MCA@900_20 electrocatalysts. Process: EO-H_2O_2 at (●) 10 mA cm^{-2}, (■) 30 mA $cm^{-2}$and (▲) 60 mA cm^{-2}; (◇) EF with 0.50 mM Fe^{2+} at 10 mA cm^{-2}; (▽) PEF with 0.50 mM Fe^{2+} and a 6 W UVA lamp at 10 mA cm^{-2}.

irradiation with a 6 W UVA lamp), regardless of the carbon material. At 10 mA cm^{-2}, the use of the MCA@900 catalyst led to a profile similar to that shown in EF, but the lowest H_2O_2 content (1.9 mM) was determined at 360 min (Fig. 5a). This is a positive finding, since it corroborates the existence of additional routes that promote the H_2O_2 decomposition via reaction (1). In particular, the UVA photons ($\lambda = 360$ nm) stimulated the continuous Fe^{2+} regeneration from photo-Fenton reaction (2), thus feeding the Fenton's reaction to eventually produce more $^{\bullet}OH$ (Moreira et al., 2017; Ye et al., 2020d).

The influence of the textural properties on the ability of the GDEs to produce H_2O_2 can be better understood by assessing the result of the same type of experiment but using different electrocatalysts. Comparing the profiles of Fig. 5a-d, the benefits derived from a larger porosity are highlighted, i.e., a greater surface area and a higher volume of micro and mesopores. As an example, in EO-H_2O_2, the MCA@900- and MCA@900_5-derived GDEs clearly yielded close H_2O_2 trends at each j value tested; however, a significant upgrade was achieved using the two samples steamed for longer time, especially the MCA@900_20. After 360 min at 10 mA cm^{-2}, the H_2O_2 concentrations attained were 5.1, 6.0, 10.9 and 13.5 mM with the MCA@900, MCA@900_5, MCA@900_10 and MCA@900_20 electrocatalyst, respectively. Based on Table 1, it can be deduced that the V_m had a greater influence on the catalyst electroactivity for oxygen reduction, since this parameter changes more substantially than V_μ and S_{QSDFT} when comparing the first three catalysts with MCA@900_20. It can thus be concluded that the greater mesoporosity was the key parameter to explain the superiority of the latter catalyst, whose better performance was confirmed in EF and PEF as well. The beneficial effects of mesoporosity on the activity and selectivity of the carbon electrocatalysts agree with those reported by other authors (Fellinger et al., 2012; Park et al., 2014).

The largest proportionality between the applied j and the accumulated H_2O_2 was clearly obtained when the MCA@900_20 electrocatalyst was used. In EO-H_2O_2 at 60 mA cm^{-2}, the final H_2O_2 contents raised from 20.3 to 22.5, 33.3 and 58.4 mM as the steam treatment became longer (Fig. 5a-d). The 6-fold increase in input current (i.e., from 10 to 60 mA cm^{-2}) caused a 4.3-fold enhancement in H_2O_2 concentration at 360 min, being lower for the other GDEs. In fact, the difference in the final H_2O_2 concentration attained with each material became more significant as the current density was increased. At 60 mA cm^{-2}, the MCA@900_20-derived GDE clearly outperformed the others, suggesting a comparatively greater stability of this electrocatalyst as the electrolytic conditions become more aggressive. This can be related to the textural properties, because a higher mesoporosity (i.e., greater presence of more open pores as compared to samples steamed for shorter time) facilitates the passage of oxygen gas through the GDE, thus preserving its mechanical stability.

The excellent electrogeneration ability of the synthesized carbons, in particular the one steamed for 20 min, is also reflected in the corresponding time course of the current efficiency (Fig. S5a-d), determined from Eq. (6). A common feature in the profiles of the four materials is the decay of the efficiency during the electrolysis. The maximum CE values were found after 30–60 min in EO-H_2O_2 process at 10–30 mA cm^{-2}, attaining 41.0%, 44.7%, 74.5% and as much as 95.3% with the MCA@900 (Fig. S5a), MCA@900_5 (Fig. S5b), MCA@900_10 (Fig. S5c) and MCA@900_20 (Fig. S5 d), respectively. Thereafter, a moderate decay led to 22.7%, 26.8%, 48.8% and 60.5% at 360 min, in agreement with the loss of H_2O_2 accumulation rate due to the enhanced parasitic reactions (Fig. 5a-d). Note that the two latter samples still kept a high efficiency, which informs about their suitability for undertaking long treatments. For the most efficient electrocatalyst (MCA@900_20), the CE at 360 min decreased from 60.5% to 48.7% and 43.4% at 10, 30 and 60 mA cm^{-2}, respectively. This means that, despite the faster rate of reaction (5) caused by the increasing j (Fig. 5a-d), the aforementioned reactions that partly wasted the generated H_2O_2 also became more significant and hence, $j = 10$ mA cm^{-2} was chosen as the optimum value for all subsequent trials. On the other hand, as commented above, the largest difference in efficiency between MCA@900_20 and the other catalysts was found at 60 mA cm^{-2}, since the CE at 360 min for these other materials could only reach half of the value or less, which confirms the greater stability of the MCA@900_20 in addition to its greater electroactivity. These findings allow corroborating the viability of agarose as the carbon source and steam treatment as a method to improve the textural properties, which have direct impact on the resistance of the material and its ability to promote reaction (5) over parasitic reactions.

In agreement with the higher destruction of H_2O_2 shown in EF and PEF (Fig. 5d), the accumulation efficiency using the MCA@900_20-derived GDE decreased down to 31.8% and 25.1% at 360 min, respectively.

In order to contextualize the H_2O_2 concentrations and current efficiencies obtained, several comparisons can be made. Fig. S6a shows the accumulation profiles in EO-H_2O_2 trials at the three j values using a GDE prepared with commercial carbon black-PTFE electrocatalyst from BASF, also on carbon cloth. At each j, the trend was very similar to that reported with the MCA@900_20 in Fig. 5d, attaining 13.1, 36.9 and 57.7 mM H_2O_2 at 360 min as j was increased. Accordingly, the CE at 10 mA cm^{-2} was 58.3%, close to 60.5% for the agarose-derived GDE (Fig. S5d). However, note that at short time the efficiency with the commercial GDE was quite lower (75.2% at 30 min, instead of 95.3% shown in Fig. S5d). Some comparison can be made with values reported in the literature as well. For example, Garza-Campos et al. (2018) prepared GDEs with mesoporous carbons synthesized from resorcinol-formaldehyde mixtures, attaining 10.9 mM H_2O_2 after 240 min at 150 mA cm^{-2} in 0.1 M Na_2SO_4 at pH 3.0. The current efficiency was around 50% at 30 min. At that time, the CE was 75% at 50 mA cm^{-2}, which is lower than the values obtained in this work (CE > 80% can be inferred at $j < 60$ mA cm^{-2} in Fig. S5d). Other studies made the H_2O_2 electrogeneration at pilot scale employing commercial GDEs prepared with carbon black. Using 25 L of a 0.050 M Na_2SO_4 solution at pH 3.0, 0.6 mM H_2O_2 (vs 5.2 mM in this work) were measured after 30 min at 30 mA cm^{-2} (Salmerón et al., 2019). In conclusion, the efficiencies achieved with the agarose-derived GDEs are similar to those reported for carbons not synthesized from biomasses, or even higher (Zhang et al., 2020). The most important observation is, in any case, that the agarose-derived GDEs are a promising alternative, especially those from MCA@900_20, to produce enough H_2O_2 that can promote the EF and PEF treatments.

3.3. Acebutolol degradation in sulfate medium using agarose-derived GDEs

The viability of PEF process to remove 0.046 mM acebutolol from 0.050 M Na_2SO_4 solutions with 0.50 mM Fe^{2+} at pH 3.0 and 10 mA cm^{-2} is compared in Fig. 6a, considering each of the four agarose-derived GDEs. Complete drug removal was achieved in all cases within few minutes, which was possible due to: (i) the continuous Fe^{2+} photoregeneration via reaction (2), which produced $^{\bullet}OH$ and fed Fenton's reaction (1), and (ii) the contribution of M($^{\bullet}OH$) formed from reaction (3). The required time for overall abatement decreased from 20 to 18, 14 and 10 min employing the MCA@900-, MCA@900_5-, MCA@900_10- and MCA@900_20-derived GDE, respectively. This confirms that the superior ability of the latter to electrogenerate H_2O_2 (Fig. 5a-d) had key influence on the $^{\bullet}OH$ generation from Fenton's reaction (1), since the faster H_2O_2 formation allowed the consumption of Fe^{2+} immediately after its regeneration, thus preventing its natural oxidation to the less active $[Fe(OH)]^{2+}$. The inset panel of Fig. 6a shows the corresponding pseudo-first-order kinetic analysis ($R^2 > 0.97$ in all cases), yielding kinetic constants (k_1) that increased as: 0.159 min^{-1} < 0.201 min^{-1} < 0.270 min^{-1} < 0.477 min^{-1}. Such linear profiles prove that the great oxidation power of PEF process arises from its ability to maintain a constant and sufficiently high concentration of strong oxidants, in particular hydroxyl radicals, thanks to the participation of UVA photons.

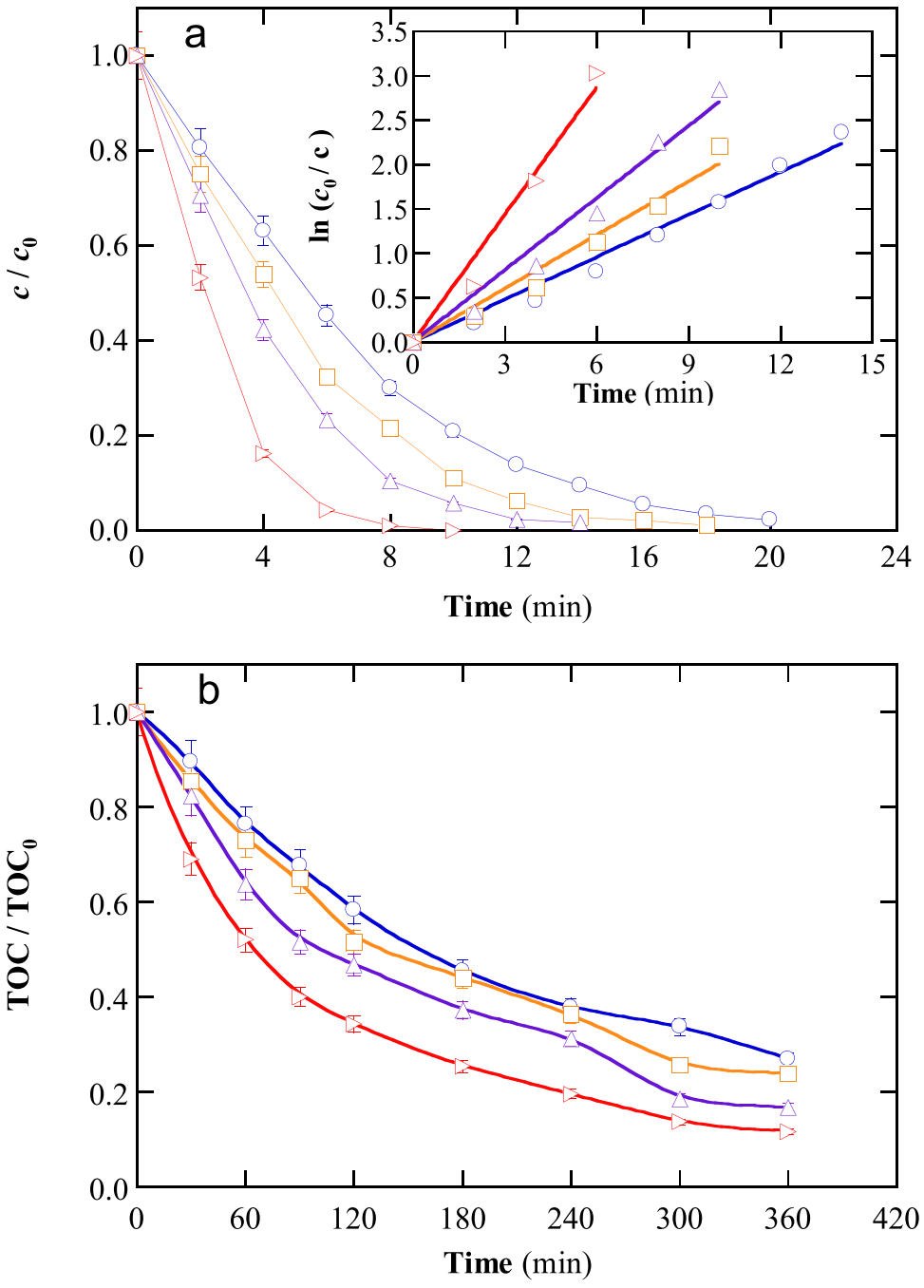

Fig. 6. (a) Time course of normalized acebutolol concentration during the PEF treatment of 150 mL of solutions containing 0.046 mM drug (10 mg L^{-1} TOC), 0.050 M Na_2SO_4 and 0.50 mM Fe^{2+} at pH 3.0, 10 mA cm^{-2} and 25 °C, using a cell with a RuO_2-based anode and a GDE as cathode prepared with (◯) MCA@900, (□) MCA@900_5, (△) MCA@900_10 and (▷) MCA@900_20 electrocatalysts. In all trials, the solution was irradiated with a 6 W UVA lamp. The inset panel shows the corresponding pseudo-first-order kinetic analysis. (b) Change of normalized TOC with electrolysis time for the same trials.

PEF clearly outperformed other widely used processes such as EO-H_2O_2 and EF, as can be seen in Fig. S7a. Despite using the best GDE, derived from the MCA@900_20 carbon, a much slower drug disappearance was obtained. In EO-H_2O_2, acebutolol degradation was only partial, reaching 34% at 120 min, owing to the absence of •OH in the bulk. Hence, the drug destruction was limited to the anode surface, where the adsorbed RuO_2(•OH) was formed via reaction (3). Since this radical interacts strongly with the anode surface, its reactivity is rather low (Martínez-Huitle et al., 2015; Lanzalaco et al., 2017). In EF, this adsorbed radical was also present, but the degradation was drastically upgraded because of the occurrence of Fenton's reaction (1). The drug concentration was totally eliminated at 20 min, thus being much slower than PEF due to the slow regeneration of Fe^{2+} at GDE (Brillas et al., 2009). In these two processes, the concentration decays also yielded pseudo first-order rate constants (linear plots with $R^2 > 0.99$). They were lower than that determined in PEF, with 3×10^{-3} min^{-1} in EO-H_2O_2 and 0.374 min^{-1} in EF, as expected from the smaller availability of hydroxyl radicals.

In Fig. 6b, the normalized TOC decays with time for the same trials of Fig. 6a are depicted. The mineralization power of PEF followed the same sequence described for the drug concentration decays, with increasing TOC removals of 73%, 76%, 83% and 90% TOC at 360 min using the

MCA@900-, MCA@900_5-, MCA@900_10- and MCA@900_20-derived GDE, respectively. Again, the enhanced textural properties of the electrocatalysts provided by prolonged steam treatment became fundamental. The large mineralization percentages can be accounted for by the aforementioned Fe^{2+} photoregeneration under UVA light, ending in a greater production of $^{\bullet}OH$ from reaction (1) that can gradually destroy the reaction products. This occurred in concomitance with the photodegradation of refractory Fe(III) complexes, typically formed with aliphatic molecules like R-COOH as the aromatic structures are broken (Steter et al., 2016; Ye et al., 2019b). An example of this kind of photoreaction is (Brillas et al., 2009; Brillas, 2020):

$$Fe(OOCR)^{2+} + h\nu \rightarrow Fe^{2+} + CO_2 + R^{\bullet} \quad (10)$$

Note that an additional positive feature of reaction (10) is that it constitutes an additional source of regenerated Fe^{2+}, thus contributing to Fenton's reaction (1). For comparison, heterogeneous photocatalysis with TiO_2 yielded 75% mineralization at 240 min (Píšťková et al., 2015), whereas at that time the use of MCA@900_20-derived GDE had caused an abatement of 80% (Fig. 6b).

The MCE for the trials of Fig. 6b was calculated from Eq. (7), considering the total mineralization reaction (8) for acebutolol. The transformation of its initial N atoms into NH_4^+ ion was hypothesized and later confirmed (subsection 3.4). Fig. S8a reveals that the PEF treatments presented the greatest efficiencies at the beginning (30–60 min), attaining 12.6%, 15.5%, 19.4% and 33.0% with the MCA@900-, MCA@900_5-, MCA@900_10- and MCA@900_20-derived GDE, respectively. The most efficient treatment involved the latter material, as expected from the more effective TOC abatement (Fig. 6b). Thereafter, all the MCE values decreased down to close values around 7–8% at 360 min. This means that once the initial products (usually aromatic, as shown below) disappear, the mineralization rate is controlled by the destruction rate of the refractory aliphatic products. These are less dependent on the applied current (i.e., the amount of $^{\bullet}OH$ and $RuO_2(^{\bullet}OH)$ formed) and are pre-eminently degraded by UVA photons, as exemplified in reaction (10). Since the irradiation was the same in the four PEF experiments, it is coherent that the MCE tended to become equal and independent of the type of GDE. An additional reason to justify the MCE decays is the loss of organic matter content, which enhances the waste of oxidants in self-decomposition reactions (Brillas et al., 2009; Martínez-Huitle et al., 2015). As a result of the efficiency loss, the energy consumption became progressively higher over time. This is evident in Fig. S8b, which shows the increasing EC_{TOC} values, determined from Eq. (9) with an average E_{cell} of 3.8 V at 10 mA cm^{-2}. Close values around 0.5–0.6 kWh (g TOC)$^{-1}$ were attained at 360 min in all cases, in agreement with the MCE similarity at the end of the electrolysis (Fig. S8a). The lowest EC_{TOC} was associated with the PEF treatment with the MCA@ 900_20 catalyst, which is another interesting result from an application point of view.

From Fig. S7a, it was discussed that PEF with MCA@900_20 was superior to EO-H_2O_2 and EF to degrade acebutolol. Such superiority was confirmed for the drug mineralization, as evidenced in Fig. S7b. A very poor TOC removal was achieved in EO-H_2O_2, reaching only 22% at 360 min. This can be explained by the low oxidation power of $RuO_2(^{\bullet}OH)$, which is unable to destroy most of the refractory aliphatic products generated upon acebutolol cleavage. The mineralization was enhanced in EF thanks to the contribution of $^{\bullet}OH$ in the bulk, although the TOC abatement at 360 min was only 62%. This value was worse than those obtained in PEF regardless of the GDE. The main reason was the accumulation of stable Fe(III) complexes with the refractory aliphatic compounds, being quite resistant to $^{\bullet}OH$ and $RuO_2(^{\bullet}OH)$ (Coria et al., 2016; Thiam et al., 2018). Based on these data, lower efficiencies were determined in EO-H_2O_2 (decreasing from 5.4% down to 2.0%) and EF (decreasing from 15.1% down to 5.5%) as compared to PEF (Fig. S9a vs. Fig. S8a). Accordingly, higher EC_{TOC} values were required (0.70 and 1.8 kWh (g TOC)$^{-1}$, respectively, at 360 min), as shown in Fig. S9b.

GDEs made with mesoporous carbons synthesized from chemicals were also employed in PEF trials with sunlight to treat 200 mL of 50 mg L^{-1} amoxicillin (Garza-Campos et al., 2018). The authors achieved the complete drug removal within 20 min using the optimum GDE. However, an incomplete TOC removal of 85% was reached at 240 min despite applying a very high j of 150 mA cm^{-2}.

3.4. Acebutolol degradation in Cl^- medium and urban wastewater using agarose-derived GDEs

The influence of an electroactive anion like Cl^- was investigated by electrolyzing 0.046 mM acebutolol (10 mg L^{-1} TOC) solutions in three different media with same conductivity as the 0.050 M Na_2SO_4 solution treated in subsection 3.3: 0.025 M Na_2SO_4 + 0.035 M NaCl, 0.070 M NaCl and urban wastewater. The cell was equipped with a RuO_2-based anode and a GDE prepared with the MCA@ 900_20 electrocatalyst, and j was 10 mA cm^{-2}. Note that the actual wastewater contained 10.4 mg L^{-1} TOC from NOM components and hence, the initial TOC in the related trials was 20.4 mg L^{-1}. Moreover, Na_2SO_4 was added at 0.050 M as an inert electrolyte in that water sample, aiming to ensure the same conductivity and discard that the possible matrix effects observed were due to a different transport by ion migration.

Fig. 7a shows the decay of the normalized acebutolol concentration over time during PEF treatments in the three matrices at pH 3.0. The complete drug disappearance required 20 min in pure chloride, 30 min in the mixed medium and up to 60 min in wastewater. All the removals were thus slower than that found in pure sulfate (10 min, Fig. 6a). This is corroborated by the good linear profiles resulting from the pseudo-first-order kinetic analysis ($R^2 > 0.99$, see inset). The k_1-values decreased as: 0.166 min^{-1} > 0.112 min^{-1} > 0.072 min^{-1}, in the three media described. These rate constants were much lower than 0.477 min^{-1} determined in pure sulfate (Fig. 6a), which informs about the detrimental effect of Cl^- ion. In 0.070 M NaCl, active chlorine (HClO as predominant species at pH 3.0) was produced from anodic Cl^- oxidation via reaction (4). This is known to be a strong oxidant that can contribute to the oxidation of aromatic pollutants (Steter et al., 2016). Nonetheless, Cl^- oxidation competes with H_2O oxidation, thus reducing the amount of the more powerful oxidant $RuO_2(^{\bullet}OH)$ generated via reaction (3). In addition, $RuO_2(^{\bullet}OH)$ and $^{\bullet}OH$ that are typically abundant in PEF were partially destroyed upon reaction with Cl^-, yielding less powerful radicals like $Cl^{\bullet}$, $ClOH^{\bullet -}$, $Cl_2^{\bullet -}$ (Steter et al., 2016). One could argue that in the presence of Fe^{2+}, a Fenton-like reaction with HClO might also yield $^{\bullet}OH$ (Steter et al., 2016), but its contribution seems of minor importance based on the rather slow acebutolol removal. In the SO_4^{2-}/Cl^- mixture, the performance of PEF was even worse because the hydroxyl radicals were partially destroyed, as just commented, and their disappearance could not be counterbalanced by the production of sufficient amounts of chlorine. Finally, the slowest drug degradation occurred in urban wastewater because of the negative effect of: (i) Cl^- ion, as explained for the two synthetic matrices; (ii) well-known radical scavengers like CO_3^{2-} and HCO_3^-, which consumed $RuO_2(^{\bullet}OH)$ and $^{\bullet}OH$ to yield the milder $CO_3^{\bullet -}$ (Ye et al., 2020a); and (iii) NOM components, which partially consumed the oxidants and UVA photons. Note also that the slightly lower transparency of the wastewater also affected negatively to acebutolol degradation, since it decelerated the photo-Fenton reaction (2).

The morphological characterization of the GDE employed for the PEF treatment in actual wastewater (Fig. 7d) can be observed in Fig. S10. The pristine material shows a reasonably good coating of the carbon cloth fibers, only exhibiting some partially uncoated ones that gives rise to the mixture of micropores and mesopores mentioned above (Fig. S10a). The electrode collected at the end of the electrolysis had a very different aspect. As shown in Fig. S10b, the continuity of the carbon film has been lost, leaving many uncoated or partially coated fibers. Despite this apparent surface degradation, the GDE was re-used with no significant change in the process performance.

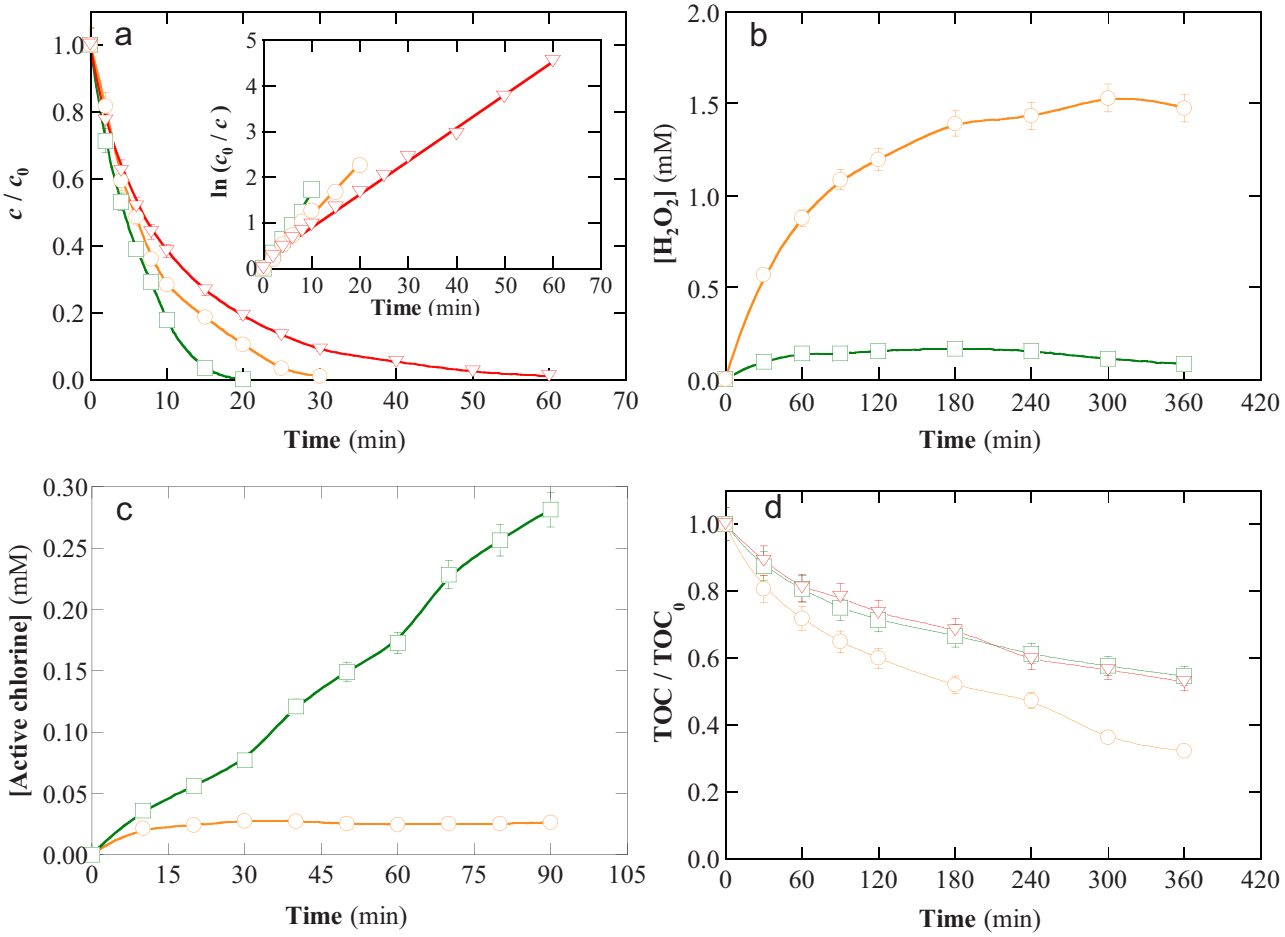

Fig. 7. (a) Time course of normalized acebutolol concentration during the PEF treatment of 150 mL of solutions containing 0.046 mM drug (10 mg L^{-1} TOC) and 0.50 mM Fe^{2+} at pH 3.0, 10 mA cm^{-2} and 25 °C, using a cell with a RuO_2-based anode and a GDE as cathode prepared with the MCA@900_20 electrocatalyst. Medium: (◯) 0.025 M Na_2SO_4 + 0.035 M NaCl, (□) 0.070 M NaCl and (▽) actual wastewater (10.4 mg L^{-1} TOC from NOM) with 0.050 M Na_2SO_4. In all trials, the solution was irradiated with a 6 W UVA lamp. The inset panel shows the corresponding pseudo-first-order kinetic analysis. Accumulated concentrations of (b) H_2O_2 and (c) active chlorine vs. time in the two synthetic media. (d) Change of normalized TOC with electrolysis time for the trials shown in plot (a).

Fig. 7b and c show the time course of accumulated H_2O_2 and active chlorine in the two synthetic media. Residual amounts of both oxidants remained in solution throughout all the electrolyses, which ensured that sufficient amounts were electrogenerated at 10 mA cm^{-2} from reactions (5) and (4), respectively. H_2O_2 concentration reached 1.5 mM in the mixed medium and 0.08 mM in pure chloride. The much lower accumulation as compared to that in sulfate medium (Fig. 5d), which was more evident in 0.070 M NaCl, was due to its partial destruction upon reaction with HClO (Steter et al., 2016). For this same reason, the active chlorine concentration in Fig. 7c was lower than expected, attaining 0.03 and 0.28 mM, respectively. The great chlorine consumption explains why this oxidant could not ensure a faster acebutolol removal (Fig. 7a).

The mineralization trends for the same three trials can be seen in Fig. 7d. At 360 min, the TOC removals were poorer than that in sulfate with MCA@900_20 (90%, Fig. 6b), owing to the smaller quantity of oxidants available upon occurrence of the various wasting reactions. Therefore, TOC was abated by 68% in the mixed medium and 45–47% in pure chloride and wastewater. The formation of relatively stable chloroorganics (see below) can be responsible for the poorer mineralization. Considering the very low input current, however, the percentage of TOC removal was quite good, since a higher j could be employed to obtain more rapid and quantitative abatements. The MCE and EC_{TOC} profiles for the trials in the two synthetic media are evidenced in Fig. S11a and b, respectively. As presumed, a lower MCE and higher EC_{TOC} were determined in comparison with PEF trial in Na_2SO_4 for the same type of GDE.

Analogous treatments of acebutolol in wastewater were also carried out in the dark with the MCA@900_20-derived GDE. Fig. S12 shows the much slower drug removal in EO-H_2O_2, only achieving 30% at 120 min ($k_1 = 3 \times 10^{-3}$ min^{-1}, see inset panel). The main oxidant under these conditions was expected to be active chlorine, but it was significantly destroyed by H_2O_2, leading to a partial concentration decay. The degradation rate was much higher in EF thanks to the $^{\bullet}OH$ produced in the bulk, although it was halved as compared to PEF ($k_1 = 0.036$ min^{-1}, with 120 min needed for 100% removal). Poor final TOC removals were observed in both cases (7% and 25%, respectively), thus corroborating the evident superiority of PEF process.

The degradation products arising from PEF treatment of solutions containing 0.046 mM drug (**1**) in 0.025 M Na_2SO_4 + 0.035 M NaCl medium with 0.50 mM Fe^{2+} at pH 3.0, 10 mA cm^{-2} and 25 °C, using a cell with a RuO_2-based anode and a GDE prepared with the MCA@900_20 electrocatalyst were analyzed by GC/MS. Two samples were collected during the electrolysis, at 20 and 60 min.

Fig. 8 shows that the reaction of **1** with active chlorine, $^{\bullet}OH$ and $RuO_2(^{\bullet}OH)$ yielded the following 12 products (main fragment ions are given), distributed in three families: (i) three non-chlorinated monobenzenes, such as 1-(2-hydroxy-5-nitrophenyl)ethan-1-one (**2**) with m/z 181, 5-hydroxy-2-methoxybenzoic acid (**3**) with m/z 168 and 2',5'-dihydroxyacetophenone (**4**) with m/z 152; (ii) six chlorinated

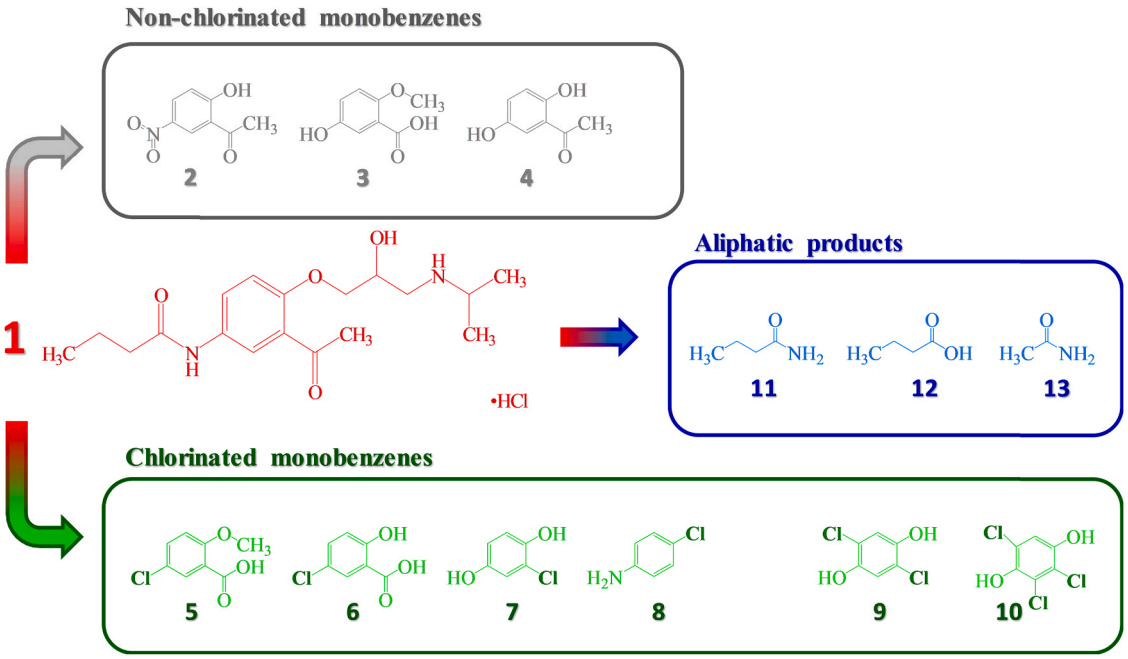

Fig. 8. Organic products of acebutolol detected by GC/MS in samples collected during the PEF treatment in 0.025 M Na_2SO_4 + 0.035 M NaCl using a GDE as cathode prepared with the MCA@900_20 electrocatalyst.

monobenzenes, including monochlorinated ones like 5-chloro-2-methoxybenzoic acid (**5**) with *m/z* 186, 5-chloro-2-hydroxybenzoic acid (**6**) with *m/z* 172, 2-chlorobenzene-1,4-diol (**7**) with *m/z* 144 and 4-chloroaniline (**8**) with *m/z* 127, as well as the two di/trichlorinated ones like 2,5-dichlorobenzene-1,4-diol (**9**) with *m/z* 178 and 3,4,5-trichlorobenzene-1,2-diol (**10**) with *m/z* 212; and (iii) three aliphatic molecules, derived from the butanamide side chain of **1**, including butanamide (**11**) with *m/z* 87, butanoic acid (**12**) with *m/z* 88 and acetamide (**13**) with *m/z* 59. The formation of the organochlorinated compounds agrees with the poorer TOC removal in the Cl^--rich matrices (Fig. 7d).

In order to quantify the main final products, PEF treatment of more concentrated (0.138 mM) acebutolol solutions was performed in 0.025 M Na_2SO_4 + 0.035 M NaCl at 10 mA cm^{-2} using the best electrocatalyst. In Fig. 9, the evolution of the concentration of two short-chain carboxylic acids is depicted. Oxalic acid reached its peak of 0.55 mg L^{-1} at 60 min, whereas that of maleic acid was 0.17 mg L^{-1} at 120 min. Thereafter, their total disappearance occurred at 240 and 360 min, respectively, thanks to the photodecarboxylation reaction (10). This means that other products like the aliphatic compounds detected by GC/MS accounted for the residual TOC shown in Fig. 6b. Fig. 9 also shows the time course of ammonium as sole nitrogenated ion

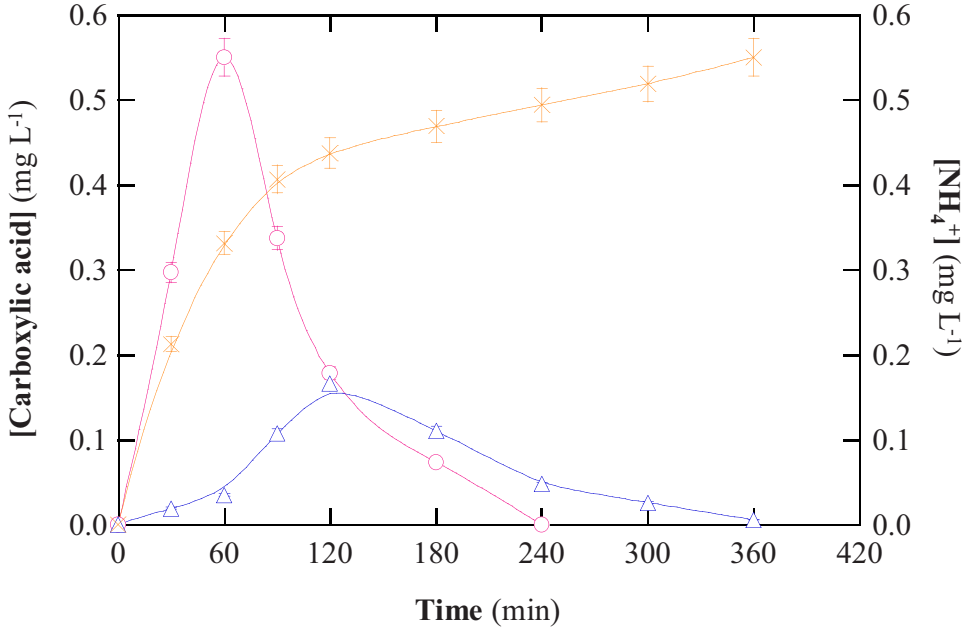

Fig. 9. Evolution of the concentration of (×) ammonium ion and (○) oxalic and (△) maleic acids during the PEF treatment of a 0.138 mM acebutolol solution with 0.025 M Na_2SO_4 + 0.035 M NaCl and 0.50 mM Fe^{2+} at pH 3.0, 10 mA cm^{-2} and 25 °C, using a cell with a RuO_2-based anode and a GDE as cathode prepared with the MCA@ 900_20 electrocatalyst. The solution was exposed to UVA light (6 W lamp).

in the same trial (see reaction (8)), since no nitrate or nitrite were identified. A steep production rate can be seen within the first hour, in agreement with the lack of N in most of the aromatic structures formed (Fig. 8). After that, the concentration increased more gradually up to 0.55 mg L^{-1} at 360 min. A *plateau* was not achieved, which means the remaining N-products (as for example the aliphatic compounds **11** and **13** of Fig. 8) became a source of ammonium. A nitrogen balance suggests that 11% of N in acebutolol was converted into dissolved N as ammonium. Hence, the rest of N yielded organic N-products and, probably, N-containing gases.

4. Conclusions

This research constitutes a step forward toward the devisal of a fully sustainable electrochemical treatment of organic pollutants in water. Agarose, an abundant and cheap biopolymer, was proven to be a suitable source of metal-free mesoporous carbon electrocatalysts. The textural properties of pyrolyzed agarose, i.e., surface area and V_m/V_μ ratio, were enhanced upon steam treatment. At an optimum duration of 20 min, the resulting MCA@ 900_20 carbon had a maximum area (1248 m^2 g^{-1}) and mesoporosity (V_m = 0.345 cm^3 g^{-1}). GDEs were then prepared with the obtained electrocatalysts to accumulate H_2O_2. With MCA@ 900_20, a current efficiency of 95.3% was reached at 30 min, outperforming a commercial GDE (75.2%). The agarose-derived electrocatalysts maintained an excellent performance upon prolonged electrolysis, showing a final efficiency close to that of commercial GDE (~60% at 360 min). The superior ability of the MCA@ 900_20-derived GDE to produce H_2O_2 as compared to the other GDEs led to a much faster acebutolol removal in PEF process. Only 10 min were needed for total degradation in sulfate medium, with 90% mineralization. EO-H_2O_2 and EF yielded slower removals, poorer TOC abatements, lower MCE and higher EC_{TOC}, owing to the absence of UV photons required to regenerate Fe^{2+}, produce more $^{\bullet}OH$ and photodecarboxylate refractory Fe(III) complexes. The drug removal was complete in synthetic media as well as in urban wastewater, with rate decreasing as: pure Cl^- > SO_4^{2-}/Cl^- > wastewater. A positive impact of active chlorine to oxidize acebutolol was observed. The formation of up to six chloro-organics in Cl^--containing medium limited the mineralization, but almost 50% TOC disappeared at 360 min in urban wastewater. The monobenzenes were progressively transformed into aliphatic products, including carboxylic acids, whose complexes with Fe(III) were totally photodecomposed. In conclusion, the in situ electrogeneration of H_2O_2 is a great advantage of EF and PEF over non-electrochemical Fenton-based processes, but its viability was considerably enhanced as the cathode was prepared from biosources.

CRediT authorship contribution statement

Yanyu Zhang: Conceptualization, Data curation, Investigation, Validation. **Giorgia Daniel:** Data curation, Investigation, Methodology, Validation. **Sonia Lanzalaco**: Formal analysis, Methodology, Writing – review & editing. **Abdirisak Ahmed Isse**; Formal analysis, Writing – review & editing. **Alessandro Facchin**: Data curation, Formal analysis. **Aimin Wang**: Funding acquisition, Writing – review & editing. **Enric Brillas**: Writing – review & editing. **Christian Durante:** Conceptualization, Methodology, Project administration, Resources, Supervision, Writing – original draft. **Ignasi Sirés:** Conceptualization, Funding acquisition, Investigation, Methodology, Project administration, Resources, Supervision, Writing – original draft.

Declaration of Competing Interest

The authors declare that they have no known competing financial interests or personal relationships that could have appeared to influence the work reported in this paper.

Acknowledgments

The authors kindly acknowledge support from projects DOR2018 (University of Padova, Italy), CTQ2016-78616-R (AEI/FEDER, EU) and PID2019-109291RB-I00 (AEI, Spain), as well as the PhD scholarship awarded to Yanyu Zhang (State Scholarship Fund, CSC, China).

Appendix A. Supporting information

Supplementary data associated with this article can be found in the online version at doi:10.1016/j.jhazmat.2021.127005.

References

Alcaide, F., Álvarez, G., Guelfi, D.R.V., Brillas, E., Sirés, I., 2020. A stable CoSP/MWCNTs air-diffusion cathode for the photoelectro-Fenton degradation of organic pollutants at pre-pilot scale. Chem. Eng. J. 379, 122417.
APWA, AWWA, WEF, 2005. Standard Methods for the Examination of Water and Wastewater, 21st ed., Method Number 4500-Cl Chlorine (residual)–G. DPD Colorimetric Method. American Public Health Association, Washington D.C., pp. 4–67–4–68
Armstrong, D.A., Huie, R.E., Koppenol, W.H., Lymar, S.V., Merényi, G., Neta, P., Ruscic, B., Stanbury, D.M., Steenken, S., Wardman, P., 2015. Standard electrode potentials involving radicals in aqueous solution: inorganic radicals (IUPAC Technical Report). Pure Appl. Chem. 87, 1139–1150.
Bagnis, S., Fitzsimons, M.F., Snape, J., Tappin, A., Comber, S., 2018. Processes of distribution of pharmaceuticals in surface freshwaters: implications for risk assessment. Environ. Chem. Lett. 16, 1193–1216.
Benner, J., Salhi, E., Ternes, T., von Gunten, U., 2008. Ozonation of reverse osmosis concentrate: kinetics and efficiency of beta blocker oxidation. Water Res. 42, 3003–3012.
Bensaadi, Z., Yeddou-Mezenner, N., Trari, M., Medjene, F., 2014. Kinetic studies of β-blocker photodegradation on TiO_2. J. Environ. Chem. Eng. 2, 1371–1377.
Beyssac, O., Goffé, B., Petitet, J.-P., Froigneux, E., Moreau, M., Rouzaud, J.-N., 2003. On the characterization of disordered and heterogeneous carbonaceous materials by Raman spectroscopy. Spectrochim. Acta A: Mol. Biomol. Spectrosc. 59, 2267–2276.
Bokobza, L., Bruneel, J.-L., Couzi, M., 2015. Raman spectra of carbon-based materials (from graphite to carbon black) and of some silicone composites. C 1, 77–94.
Borghei, M., Lehtonen, J., Liu, L., Rojas, O.J., 2018. Advanced biomass-derived electrocatalysts for the oxygen reduction reaction. Adv. Mater. 30, 1703691.
Brandiele, R., Zerbetto, M., Dalconi, M.C., Rizzi, G.A., Isse, A.A., Durante, C., Gennaro, A., 2019. Mesoporous carbon with different density of thiopheniclike functional groups and their effect on oxygen reduction. ChemSusChem 12, 4229–4239.
Brillas, E., 2020. A review on the photoelectro-Fenton process as efficient electrochemical advanced oxidation for wastewater remediation. Treatment with UV light, sunlight, and coupling with conventional and other photo-assisted advanced technologies. Chemosphere 250, 126198.
Brillas, E., Sirés, I., Oturan, M.A., 2009. Electro-Fenton process and related electrochemical technologies based on Fenton's reaction chemistry. Chem. Rev. 109, 6570–6631.
Bussy, U., Ferchaud-Roucher, V., Tea, I., Krempf, M., Silvestre, V., Boujtita, M., 2012. Electrochemical oxidation behavior of acebutolol and identification of intermediate species by liquid chromatography and mass spectrometry. Electrochim. Acta 69, 351–357.
Chen, Y., Wang, M., Tian, M., Zhu, Y., Wei, X., Jiang, T., Gao, S., 2017. An innovative electro-Fenton degradation system self-powered by triboelectric nanogenerator using biomass-derived carbon materials as cathode catalyst. Nano Energy 42, 314–321.
Coria, G., Sirés, I., Brillas, E., Nava, J.L., 2016. Influence of the anode material on the degradation of naproxen by Fenton-based electrochemical processes. Chem. Eng. J. 304, 817–825.
Cychosz, K.A., Guillet-Nicolas, R., García-Martínez, J., Thommes, M., 2017. Recent advances in the textural characterization of hierarchically structured nanoporous materials. Chem. Soc. Rev. 46, 389–414.
Daniel, G., Foltran, E., Brandiele, R., Nodari, L., Pilot, R., Menna, E., Rizzi, G.A., Isse, A. A., Durante, C., Gennaro, A., 2018. Platinum-free electrocatalysts for oxygen reduction reaction: Fe-N_x modified mesoporous carbon prepared from biosources. J. Power Sources 402, 434–446.
Daniel, G., Zhang, Y., Lanzalaco, S., Brombin, F., Kosmala, T., Granozzi, G., Wang, A., Brillas, E., Sirés, I., Durante, C., 2020. Chitosan-derived nitrogen-doped carbon electrocatalyst for a sustainable upgrade of oxygen reduction to hydrogen peroxide in UV-assisted electro-Fenton water treatment. ACS Sustain. Chem. Eng. 8, 14425–14440.
Desbiolles, F., Malleret, L., Tiliacos, C., Wong-Wah-Chung, P., Laffont-Schwob, I., 2018. Occurrence and ecotoxicological assessment of pharmaceuticals: is there a risk for the Mediterranean aquatic environment? Sci. Total Environ. 639, 1334–1348.
Dong, K., Lei, Y., Zhao, H., Liang, J., Ding, P., Liu, Q., Xu, Z., Lu, S., Li, Q., Sun, X., 2020. Noble-metal-free electrocatalysts toward H_2O_2 production. J. Mater. Chem. A 8, 23123–23141.

Espinoza, L.C., Sepúlveda, P., García, A., Martins de Godoi, D., Salazar, R., 2020. Degradation of oxamic acid using dimensionally stable anodes (DSA) based on a mixture of RuO_2 and IrO_2 nanoparticles. Chemosphere 251, 126674.
Favaro, M., Carraro, F., Cattelan, M., Colazzo, L., Durante, C., Sambi, M., Gennaro, A., Agnoli, S., Granozzi, G., 2015a. Multiple doping of graphene oxide foams and quantum dots: new switchable systems for oxygen reduction and water remediation. J. Mater. Chem. A 3, 14334–14347.
Favaro, M., Ferrighi, L., Fazio, G., Colazzo, L., Valentin, C.Di, Durante, C., Sedona, F., Gennaro, A., Agnoli, S., Granozzi, G., 2015b. Single and multiple doping in graphene quantum dots: unraveling the origin of selectivity in the oxygen reduction reaction. ACS Catal. 5, 129–144.
Fellinger, T.-P., Hasché, F., Strasser, P., Antonietti, M., 2012. Mesoporous nitrogen-doped carbon for the electrocatalytic synthesis of hydrogen peroxide. J. Am. Chem. Soc. 134, 4072–4075.
Ferrari, A.C., Robertson, J., 2000. Interpretation of Raman spectra of disordered and amorphous carbon. Phys. Rev. B 61, 14095–14107.
Fraysse, B., Garric, J., 2005. Prediction and experimental validation of acute toxicity of β-blockers in *Ceriodaphnia dubia*. Environ. Toxicol. Chem. 24, 2470–2476.
Ganiyu, S.O., Huong T.X., Le, Bechelany, M., Oturan, N., Papirio, S., Esposito, G., van Hullebusch, E., Cretin, M., Oturan, M.A., 2018a. Electrochemical mineralization of sulfamethoxazole over wide pH range using $Fe^{II}Fe^{III}$ LDH modified carbon felt cathode: degradation pathway, toxicity and reusability of the modified cathode. Chem. Eng. J. 350, 844–855.
Ganiyu, S.O., Zhou, M., Martínez-Huitle, C.A., 2018b. Heterogeneous electro-Fenton and photoelectro-Fenton processes: a critical review of fundamental principles and application for water/wastewater treatment. Appl. Catal. B: Environ. 235, 103–129.
Garza-Campos, B., Morales-Acosta, D., Hernández-Ramírez, A., Guzmán-Mar, J.L., Hinojosa-Reyes, L., Manríquez, J., Ruiz-Ruiz, E.J., 2018. Air diffusion electrodes based on synthetized mesoporous carbon for application in amoxicillin degradation by electro-Fenton and solar photo electro-Fenton. Electrochim. Acta 269, 232–240.
Godoy, A.A., Kummrow, F., Pamplin, P.A.Z., 2015. Occurrence, ecotoxicological effects and risk assessment of antihypertensive pharmaceutical residues in the aquatic environment – a review. Chemosphere 138, 281–291.
Hammouda, S.B., Salazar, C., Zhao, F., Lakshami Ramasamy, D., Laklova, E., Iftekhar, S., Babu, I., Sillanpää, M., 2019. Efficient heterogeneous electro-Fenton incineration of a contaminant of emergent concern-cotinine- in aqueous medium using the magnetic double perovskite oxide Sr_2FeCuO_6 as a highly stable catalyst: Degradation kinetics and oxidation products. Appl. Catal. B: Environ. 240, 201–214.
Huong Le, T.X., Bechelany, M., Cretin, M., 2017. Fe-Nanoporous carbon derived from MIL-53(Fe): a heterogeneous catalyst for mineralization of organic pollutants. Carbon 122, 564–591.
Jaouen, F., Lefèvre, M., Dodelet, J.-P., Cai, M., 2006. Heat-treated Fe/N/C catalysts for O_2 electroreduction: are active sites hosted in micropores? J. Phys. Chem. B 110, 5553–5558.
Javhori, T., Roid, A., Casado, J., 1995. Raman spectroscopic characterization of some commercially available carbon black materials. Carbon 33, 1451–1465.
Jia, N., Yang, T., Shi, S., Chen, X., An, Z., Chen, Y., Yin, S., Chen, P., 2020. N,F-Co-doped carbon nanocages: an efficient electrocatalyst for hydrogen peroxide electroproduction in alkaline and acidic solutions. ACS Sustain. Chem. Eng. 8, 2883–2891.
Jirkovský, J.S., Björling, A., Ahlberg, E., 2012. Reduction of oxygen on dispersed nanocrystalline CoS_2. J. Phys. Chem. C 116, 24436–24444.
Khalit, W.N.A.W., Tay, K.S., 2016. Aqueous chlorination of acebutolol: kinetics, transformation by-products, and mechanism. Environ. Sci. Pollut. Res. 23, 2521–2529.
Lanzalaco, S., Sirés, I., Sabatino, M.A., Dispenza, C., Scialdone, O., Galia, A., 2017. Synthesis of polymer nanogels by electro-Fenton process: investigation of the effect of main operation parameters. Electrochim. Acta 246, 812–822.
Larsson, D.G.K., 2014. Pollution from drug manufacturing: review and perspectives. Philos. Trans. R. Soc. Lond. B Biol. Sci. 369, 20130571.
Lee, S.H., Kim, J., Chung, D.Y., Yoo, J.M., Lee, H.S., Kim, M.J., Mun, B.S., Kwon, S.G., Sung, Y.-E., Hyeon, T., 2019. Design principle of Fe-N-C electrocatalysts: How to optimize multimodal porous structures? J. Am. Chem. Soc. 141, 2035–2045.
Liao, M.-J., Wang, Y.-L., Li, S.-S., Li, J.-F., Chen, P., 2019. Electrocatalyst derived from abundant biomass and its excellent activity for in situ H_2O_2 production. ChemElectroChem 6, 4877–4884.
Liu, F., Liu, L., Li, X., Zeng, J., Du, L., Liao, S., 2016. Nitrogen self-doped carbon nanoparticles derived from spiral seaweeds for oxygen reduction reaction. RSC Adv. 6, 27535–27541.
Lu, Z., Chen, G., Siahrostami, S., Chen, Z., Liu, K., Xie, J., Liao, L., Wu, T., Lin, D., Jaramillo, T.F., Nørskov, J.K., Cui, Y., 2018. High-efficiency oxygen reduction to hydrogen peroxide catalysed by oxidized carbon materials. Nat. Catal. 1, 156–162.
Madrid, E., Lowe, J.P., Msayib, K.J., McKeown, N.B., Song, Q., Attard, G.A., Düren, F., Marken, F., 2019. Triphasic nature of polymers of intrinsic microporosity induces storage and catalysis effects in hydrogen and oxygen reactivity at electrode surfaces. ChemElectroChem 6, 252–259.
Martínez-Huitle, C.A., Rodrigo, M.A., Sirés, I., Scialdone, O., 2015. Single and coupled electrochemical processes and reactors for the abatement of organic water pollutants: a critical review. Chem. Rev. 115, 13362–13407.
Monteil, H., Péchaud, Y., Oturan, N., Trellu, C., Oturan, M.A., 2019. A review on efficiency and cost effectiveness of electro- and bio-electro-Fenton processes: application to the treatment of pharmaceutical pollutants in water. Chem. Eng. J. 376, 119577.
Moreira, F.C., Boaventura, R.A.R., Brillas, E., Vilar, V.J.P., 2017. Electrochemical advanced oxidation processes: a review on their application to synthetic and real wastewaters. Appl. Catal. B: Environ. 202, 217–261.
Olvera-Vargas, H., Gore-Datar, N., Garcia-Rodriguez, O., Mutnuri, S., Lefebvre, O., 2020. Electro-Fenton treatment of real pharmaceutical wastewater paired with a BDD anode: reaction mechanisms and respective contribution of homogeneous and heterogeneous $^{\bullet}OH$. Chem. Eng. J. 404, 126524.
Park, J., Nabae, Y., Hayakawa, T., Kakimoto, M.-A., 2014. Highly selective two-electron oxygen reduction catalyzed by mesoporous nitrogen-doped carbon. ACS Catal. 4, 3749–3754.
Perazzolo, V., Durante, C., Gennaro, A., 2016a. Nitrogen and sulfur doped mesoporous carbon cathodes for water treatment. J. Electroanal. Chem. 782, 264–269.
Perazzolo, V., Durante, C., Pilot, R., Paduano, A., Zheng, J., Rizzi, G.A., Martucci, A., Granozzi, G., Gennaro, A., 2015. Nitrogen and sulfur doped mesoporous carbon as metal-free electrocatalysts for the in situ production of hydrogen peroxide. Carbon 95, 949–963.
Perazzolo, V., Grądzka, E., Durante, C., Pilot, R., Vicentini, N., Rizzi, G.A., Granozzi, G., Gennaro, A., 2016b. Chemical and electrochemical stability of nitrogen and sulphur doped mesoporous carbons. Electrochim. Acta 197, 251–262.
Pérez-Ramírez, J., Verboekend, D., Bonilla, A., Abelló, S., 2009. Zeolite catalysts with tunable hierarchy factor by pore-growth moderators. Adv. Funct. Mater. 19, 3972–3979.
Píšťková, V., Tasbihi, M., Vávrová, M., Štangar, U.L., 2015. Photocatalytic degradation of β-blockers by using immobilized titania/silica on glass slides. J. Photochem. Photobiol. A: Chem. 305, 19–28.
Pizzutilo, E., Kasian, O., Choi, C.H., Cherevko, S., Hutchings, G.J., Mayrhofer, K.J.J., Freakley, S.J., 2017. Electrocatalytic synthesis of hydrogen peroxide on Au-Pd nanoparticles: from fundamentals to continuous production. Chem. Phys. Lett. 683, 436–442.
Qin, M., Fan, S., Wang, L., Gan, G., Wang, X., Cheng, J., Hao, Z., Li, X., 2020. Oxygen and nitrogen co-doped ordered mesoporous carbon materials enhanced the electrochemical selectivity of O_2 reduction to H_2O_2. J. Colloid Interface Sci. 562, 540–549.
Sadezky, A., Muckenhuber, H., Grothe, H., Niessner, R., Pöschl, U., 2005. Raman microspectroscopy of soot and related carbonaceous materials: spectral analysis and structural information. Carbon 43, 1731–1742.
Salmerón, I., Plakas, K.V., Sirés, I., Oller, I., Maldonado, M.I., Karabelas, A.J., Malato, S., 2019. Optimization of electrocatalytic H_2O_2 production at pilot plant scale for solar-assisted water treatment. Appl. Catal. B: Environ. 242, 327–336.
Shi, R., Shang, L., Zhang, T., 2021. Three phase interface engineering for advanced catalytic applications. ACS Appl. Energy Mater. 4, 1045–1052.
Singh, R., Bhattacharya, B., Tomar, S.K., Singh, V., Singh, P.K., 2017. Electrical, optical and electrophotochemical studies on agarose based biopolymer electrolyte towards dye sensitized solar cell application. Measurement 102, 214–219.
Steter, J.R., Brillas, E., Sirés, I., 2016. On the selection of the anode material for the electrochemical removal of methylparaben from different aqueous media. Electrochim. Acta 222, 1464–1474.
Thiam, A., Salazar, R., Brillas, E., Sirés, I., 2018. Electrochemical advanced oxidation of carbofuran in aqueous sulfate and/or chloride media using a flow cell with a RuO_2-based anode and an air-diffusion cathode at pre-pilot scale. Chem. Eng. J. 335, 133–144.
Tian, M., Zhu, Y., Zhang, D., Wang, M., Chen, Y., Yang, Y., Gao, S., 2019. Pyrrolic-nitrogen-rich biomass-derived catalyst for sustainable degradation of organic pollutant via a self-powered electro-Fenton process. Nano Energy 64, 103940.
Vadodariya, N., Chaudhary, Prakash, Raval, J., Meena, R, H.D., 2018. Graded agaroses directly from seaweed biomass: a sustainable tool for developing clean chemical process. Process Biochem 66, 171–175.
Vasconcelos, V.M., Ponce-de-León, C., Nava, J.L., Lanza, M.R.V., 2016. Electrochemical degradation of RB-5 dye by anodic oxidation, electro-Fenton and by combining anodic oxidation–electro-Fenton in a filter-press flow cell. J. Electroanal. Chem. 765, 179–187.
Wang, Y., Shi, R., Shang, L., Waterhouse, G.I.N., Zhao, J., Zhang, Q., Gu, L., Zhang, T., 2020. High-efficiency oxygen reduction to hydrogen peroxide catalyzed by nickel single-atom catalysts with tetradentate N_2O_2 coordination in a three-phase flow cell. Angew. Chem. Int. Ed. 59, 13057–13062.
Welcher, F.J., 1975. Standard Methods of Chemical Analysis, sixth ed.,. R.E. Krieger Publishing Co, Huntington, New York (Part B).
Wen, Z., Wang, A., Zhang, Y., Ren, S., Tian, X., Li, J., 2019. Mineralization of cefoperazone in acid medium by the microwave discharge electrodeless lamp irradiated photoelectro-Fenton using a RuO_2/Ti or boron-doped diamond anode. J. Hazard. Mater. 374, 186–194.
Xia, C., Kim, J.Y., Wang, H., 2020. Recommended practice to report selectivity in electrochemical synthesis of H_2O_2. Nat. Catal. 3, 605–607.
Xu, Z., Zhao, H., Liang, J., Wang, Y., Li, T., Luo, Y., Shi, X., Lu, S., Feng, Z., Wu, Q., Sun, X., 2020. Noble-metal-free electrospun nanomaterials as electrocatalysts for oxygen reduction reaction. Mater. Today Phys. 15, 100280.
Yang, W., Du, Z., Ma, Z., Wang, G., Bai, H., Shao, G., 2016. Facile synthesis of nitrogen-doped hierarchical porous lamellar carbon for high-performance supercapacitors. RSC Adv. 6, 3942–3950.
Yang, H., Zhou, M., Yang, W., Ren, G., Ma, L., 2018. Rolling-made gas diffusion electrode with carbon nanotube for electro-Fenton degradation of acetylsalicylic acid. Chemosphere 206, 439–446.
Yang, W., Zhou, M., Oturan, N., Bechelany, M., Cretin, M., Oturan, M.A., 2020. Highly efficient and stable $Fe^{II}Fe^{III}$ LDH carbon felt cathode for removal of pharmaceutical ofloxacin at neutral pH. J. Hazard. Mater. 393, 122513.
Yang, W., Zhou, M., Oturan, N., Li, Y., Oturan, M.A., 2019. Electrocatalytic destruction of pharmaceutical imatinib by electro-Fenton process with graphene-based cathode. Electrochim. Acta 305, 285–294.

Yang, Y., He, F., Shen, Y., Chen, X., Mei, H., Liu, S., Zhang, Y., 2017. A biomass derived N/C-catalyst for the electrochemical production of hydrogen peroxide. Chem. Commun. 53, 9994–9997.

Ye, Z., Brillas, E., Centellas, F., Cabot, P.L., Sirés, I., 2019a. Electro-Fenton process at mild pH using Fe(III)-EDDS as soluble catalyst and carbon felt as cathode. Appl. Catal. B: Environ. 257, 117907.

Ye, Z., Brillas, E., Centellas, F., Cabot, P.L., Sirés, I., 2020a. Expanding the application of photoelectro-Fenton treatment to urban wastewater using the Fe(III)-EDDS complex. Water Res 169, 115219.

Ye, Z., Guelfi, D.R.V., Álvarez, G., Alcaide, F., Brillas, E., Sirés, I., 2019b. Enhanced electrocatalytic production of H_2O_2 at Co-based air-diffusion cathodes for the photoelectro-Fenton treatment of bronopol. Appl. Catal. B: Environ. 247, 191–199.

Ye, Z., Padilla, J.A., Xuriguera, E., Beltran, J.L., Alcaide, F., Brillas, E., Sirés, I., 2020b. A highly stable metal–organic framework-engineered FeS_2/C nanocatalyst for heterogeneous electro-Fenton treatment: validation in wastewater at mild pH. Environ. Sci. Technol. 54, 4664–4674.

Ye, Z., Padilla, J.A., Xuriguera, E., Brillas, E., Sirés, I., 2020c. Magnetic MIL (Fe)-type MOF-derived N-doped nano-ZVI@C rods as heterogeneous catalyst for the electro-Fenton degradation of gemfibrozil in a complex aqueous matrix. Appl. Catal. B: Environ. 266, 118604.

Ye, Z., Schukraft, G.E.M., L'Hermitte, A., Xiong, Y., Brillas, E., Petit, C., Sirés, I., 2020d. Mechanism and stability of an Fe-based 2D MOF during the photoelectro-Fenton treatment of organic micropollutants under UVA and visible light irradiation. Water Res 184, 115986.

Zhang, H., Li, Y., Zhao, Y., Li, G., Zhang, F., 2019. Carbon black oxidized by air calcination for enhanced H_2O_2 generation and effective organics degradation. ACS Appl. Mater. Interfaces 11, 27846–27853.

Zhang, Q., Zhou, M., Ren, G., Li, Y., Li, Y., Du, X., 2020. Highly efficient electrosynthesis of hydrogen peroxide on a superhydrophobic three-phase interface by natural air diffusion. Nat. Commun. 11, 1731.